The Astrophysical Journal, 905:52 (19pp), 2020 December 10 https://doi.org/10.3847/1538-4357/abc2ce

High-redshift Extreme Variability Quasars from Sloan Digital Sky Survey Multiepoch Spectroscopy

Hengxiao Guo (郭恒潇)[1,2,3,12], Jiacheng Peng[4], Kaiwen Zhang[5], Colin J. Burke[1,2], Xin Liu[1,2], Mouyuan Sun[6], Shu Wang[7,8], Minzhi Kong[4,12], Zhenfeng Sheng[9,10], Tinggui Wang[9,10], Zhicheng He[9,10], and Minfeng Gu[11]
[1] Department of Astronomy, University of Illinois at Urbana-Champaign, Urbana, IL 61801, USA; hengxiaoguo@gmail.com, confucious_76@163.com
[2] National Center for Supercomputing Applications, University of Illinois at Urbana-Champaign, Urbana, IL 61801, USA
[3] Department of Physics and Astronomy, 4129 Frederick Reines Hall, University of California, Irvine, CA, 92697-4575, USA
[4] Department of Physics, Hebei Normal University, No. 20 East of South 2nd Ring Road, Shijiazhuang 050024, People's Republic of China
[5] Department of Physics, University of Illinois at Urbana-Champaign, 1110 West Green Street, Urbana, IL 61801, USA
[6] Department of Astronomy, Xiamen University, Xiamen, Fujian 361005, People's Republic of China
[7] Kavli Institute for Astronomy and Astrophysics, Peking University, Beijing 100871, People's Republic of China
[8] Department of Astronomy, School of Physics, Peking University, Beijing 100871, People's Republic of China
[9] CAS Key Laboratory for Researches in Galaxies and Cosmology, University of Sciences and Technology of China, Hefei, Anhui 230026, People's Republic of China
[10] School of Astronomy and Space Science, University of Science and Technology of China, Hefei 230026, People's Republic of China
[11] Key Laboratory for Research in Galaxies and Cosmology, Shanghai Astronomical Observatory, Chinese Academy of Sciences, 80 Nandan Road, Shanghai 200030, People's Republic of China
Received 2020 June 14; revised 2020 September 16; accepted 2020 October 12; published 2020 December 11

Abstract

We perform a systematic search for high-redshift ($z > 1.5$) extreme variability quasars (EVQs) using repeat spectra from the Sixteenth Data Release of the Sloan Digital Sky Survey, which provides a baseline spanning up to ∼18 yr in the observed frame. We compile a sample of 348 EVQs with a maximum continuum variability at rest frame 1450 Å of more than 100% (i.e., $\delta V \equiv (\mathrm{Max} - \mathrm{Min})/\mathrm{Mean} > 1$). The EVQs show a range of emission-line variability, including 23 where at least one line in our redshift range disappears below detectability, which can then be seen as analogous to low-redshift changing-look quasars (CLQs). Importantly, spurious CLQs caused by problematic SDSS spectral flux calibration, e.g., fiber-drop issue, have been rejected. The similar properties (e.g., continuum/line, difference-composite spectra and Eddington ratio) of normal EVQs and CLQs imply that they are basically the same physical population with analogous intrinsic variability mechanisms, as a tail of a continuous distribution of normal quasar properties. In addition, we find no reliable evidence ($\lesssim 1\sigma$) to support that CLQs are a subset of EVQs with less efficient accretion. Finally, we also confirm the antibreathing of C IV (i.e., the line width increases as luminosity increases) in EVQs and find that in addition to the ∼0.4 dex systematic uncertainty in single-epoch C IV virial black hole mass estimates, an extra scatter of ∼0.3 dex will be introduced by extreme variability.

Unified Astronomy Thesaurus concepts: Active galactic nuclei (16); Quasars (1319); Black hole physics (159); Spectroscopy (1558); Time domain astronomy (2109)

Supporting material: machine-readable table

1. Introduction

The canonical unification scheme of active galactic nuclei (AGNs)[13] dictates that broad-line (Type 1) and narrow-line (Type 2) objects are the same underlying population viewed at different orientations (Antonucci 1993; Urry & Padovani 1995). The discovery of a rare changing-look (CL; or "changing-state") phenomenon where an AGN changes type and exhibits flux variations of more than a factor of a few with significantly enhanced (or reduced) broad emission-line flux over months to decades (e.g., Tohline & Osterbrock 1976; Cohen et al. 1986; Aretxaga et al. 1999; Denney et al. 2014; Shappee et al. 2014; LaMassa et al. 2015; MacLeod et al. 2016; Ruan et al. 2016a; Runco et al. 2016; Runnoe et al. 2016; Yang et al. 2018; Guo et al. 2019; Trakhtenbrot et al. 2019; Ai et al. 2020; Sheng et al. 2020) challenges this simple unification picture.

Dust obscuration, whereby broad-line-region (BLR) clouds move in and out of the line of sight, should be a good explanation for the CL behavior given their comparable timescales. Indeed, the dust obscuration scenario has been invoked in some earlier cases (e.g., NGC 7603, Mrk 993; Goodrich 1989; Tran et al. 1992). However, measurements of the low polarization (<1%) of CLQs (Hutsemékers et al. 2017, 2019) disfavor the obscuration picture. In addition, Sheng et al. (2017) observed large mid-infrared variability in 10 CLQs that echoes their optical variability with a time lag expected from dust reprocessing, also supporting the idea that the CL phenomenon is due to physical changes in the accretion disk or accretion rate. Meanwhile, MacLeod et al. (2019) suggest that the CL phenomenon in general is probably not due to tidal disruption events or microlensing by foreground stars, unless these events are strongly preferred in quasars with lower Eddington ratios.

To date, over 100 CLQs have been discovered with photometric and spectroscopic methods (e.g., Yang et al. 2018; MacLeod et al. 2019). Most of those observations only reveal the appearance/disappearance of broad Balmer lines (e.g., Hβ or Hα), while the transition of broad Mg II is rarely observed even in the dim state (Homan et al. 2020). Roig et al. (2014)

[12] Corresponding author.
[13] Throughout this paper, the terms AGN and quasar are used interchangeably regardless of the luminosity difference.

noticed some unusual Mg II emitters that show strong and broad Mg II lines, but very weak or unrecognizable emission in other normal indicators of AGN activity, such as Hα, Hβ, and the near-UV power-law continuum. Thanks to the discovery of Mg II emitters, Guo et al. (2019) discovered the first Mg II CLQ based on the repeat observations of 361 Mg II emitters in SDSS DR14. However, the CL phenomenon at high redshift (e.g., $z > 1.5$) has barely been explored (Ross et al. 2020), and the transition behaviors of different UV emission lines are still unclear.

The primary approaches to search for CLQs are photometric and spectroscopic methods. However, their behavior is not always associated. On one hand, previous studies have used their extremely variable nature to search for CLQs (Graham et al. 2020; Yang et al. 2020). For instance, MacLeod et al. (2016) found that most of their ~1000 photometrically selected objects with variations of $|\Delta g| > 1$ mag are EVQs rather than CLQs (only 10 confirmed CLQs). On the other hand, 15 CLQs selected from repeat SDSS (SDSS/LAMOST) spectra show dispersed variabilities ranging from 0.03 to 1.59 mag in the g band with a median of 0.3 mag (Yang et al. 2018). Furthermore, J1525+2920, the Mg II CLQ in Guo et al. (2019), exhibits small variability of only 0.1 mag in its g-band light curve. This clearly indicates that large photometric variability does not guarantee CL behavior, and the real CL phenomenon does occur with inconspicuous variability. Therefore, searching for CLQs with repeat spectra is more straightforward given the advent of powerful modern spectroscopic surveys such as the Time-Domain Spectroscopic Survey (TDSS; Ruan et al. 2016b), SDSS-V (Kollmeier et al. 2017), the Large Sky Area Multi-Object Fiber Spectroscopic Telescope (LAMOST; Cui et al. 2012), and the forthcoming Dark Energy Spectroscopic Instrument (DESI; DESI Collaboration et al. 2016). In addition, the delayed follow-up of photometrically selected candidates may miss the best opportunity to capture the faintest state.

According to the expectation of the photoionization model, if the continuum luminosity decreases continuously, all the broad emission lines (e.g., C IV, C III] and Mg II) will gradually fade away and finally be swamped by spectral noise as a CLQ (Guo et al. 2020). Therefore, the purpose of this paper is as follows:

1. Compile a sample of high-redshift EVQs and identify new CLQs with transitions in different emission lines (e.g., C IV and C III]).
2. Explore the prerequisites for CL behaviors (e.g., critical Eddington ratios).
3. Check the relationship between CLQs and EVQs in the AGN family and try to understand their intrinsic variability mechanism.

The paper is organized as follows. In Section 2, we describe the data set of photometries and spectroscopies used to identify EVQs/CLQs. In Section 3, we illustrate the sample selections of the high-redshift EVQs/CLQs and reject spurious EVQs/CLQs caused by SDSS fiber dropping. Then, we compare the properties of the non-CL EVQs and CLQs in our total EVQ sample to explore the prerequisites of CL behaviors in Section 4. In Section 5, we discuss the CL behavior, the intrinsic variability mechanism of EVQs/CLQs, and the single-epoch black hole (BH) mass estimated from C IV in EVQs. Finally, we draw our conclusions in Section 6. A concordance ΛCDM cosmology with $\Omega_m = 0.3$, $\Omega_\Lambda = 0.7$, and $H_0 = 70$ km s^{-1} Mpc^{-1} is assumed throughout.

2. Data

Repeat SDSS spectra with a baseline of up to 18 yr is an ideal tool to identify CL behavior, while photometric light curves are expected to verify the concurrent spectral variability. There is no current single survey that has sufficient sky coverage, baseline, depth, and cadence to support a verification of CLQs (targets of opportunity). Therefore, the best strategy is to combine different surveys (e.g., CRTS and PTF/iPTF/ZTF) to extend the baseline and gain to as high a cadence as possible to trace the transition in CLQs with a typical timescale of months to decades.

2.1. SDSS Spectrum

All the spectra in this work are obtained from the public Sixteenth Data Release of Sloan Digital Sky Survey (SDSS DR16) database (Ahumada et al. 2020), which covers 14,555 deg^2, mostly in the northern sky. DR16 is also notable as the final data release from the Extended Baryon Oscillation Spectroscopic Survey (eBOSS; Dawson et al. 2016). Benefiting from its cumulative data archive from 2000 to the present, many objects have been observed more than once. This is quite suitable for investigating AGN spectral variability and searching for CLQs. The repeat spectroscopic observations are mainly from three parts: (1) the overlapped survey areas between adjacent plates; (2) dedicated programs, e.g., TDSS (Ruan et al. 2016b) and SDSS reverberation mapping (SDSS-RM, Shen et al. 2015); and (3) plates reobserved due to insufficient signal-to-noise ratio (S/N). The spectral wavelength coverage for SDSS I and II (SDSS III and IV) is 3800–9200 (3600–10400) Å with spectral resolution $R \sim$ 1850–2200.

The asserted accuracy of absolute spectral flux calibration of stars is about 6%[14] after SDSS III with a 2″ fiber size. Compared to the calibration algorithm in DR14, DR16 used a new set of stellar templates to fit absorption lines of standard stars, which reduces residuals by a factor of 2 in the blue spectrograph (3600–6000 Å) relative to previous releases through improved modeling of spectral lines in F-stars. However, comparison between repeat observations indicates the precision of spectral flux calibration is significantly underestimated in high-redshift quasars (see details in Appendix A).

2.2. CRTS

The Catalina Real-Time Transient Survey (CRTS; Drake et al. 2009) is a ~33,000 deg^2 survey designed to discover rare and interesting transients (e.g., supernovae, TDEs, and CLQs). It was conducted with three 1 m class telescopes in both Northern and Southern Hemispheres—the 0.7 m Catalina Sky Survey (CSS) Schmidt, the 1.5 m Mount Lemmon Survey (MLS) telescopes in Arizona, and the 0.5 m Siding Springs Survey (SSS) Schmidt in Australia. CRTS covers up to ~2500 deg^2 per night, with four exposures per visit, separated by 10 minutes. It contains time series for approximately 500 million sources with a limiting magnitude of $V \sim 21$ mag (Vega system) from 2003 to 2016. All the data are automatically processed in real time to report potential transients. All photometries are aperture based and broadly calibrated to Johnson V (Drake et al. 2013).

[14] https://www.sdss.org/dr16/algorithms/spectrophotometry/

2.3. PTF, iPTF, and ZTF

The Palomar Transient Factory (PTF) is a fully automated, wide-field, time-domain survey designed to explore the transient and variable sky conducted from 2009 to 2012 (Law et al. 2009; Rau et al. 2009). The observations are made at Palomar Observatory with the 48 inch (P48, 1.2 m) Samuel Oschin Schmidt telescope equipped with the CHF12K camera. It covers ∼3000 deg^2 of the northern sky with a 5σ limiting AB magnitude of ∼20.6 in Mould $-R$ and ∼21.3 in SDSS g bands with an average 5 day cadence. The intermediate Palomar Transient Factory (iPTF) ran from 2013 to 2017 as the successor to the PTF on P48 telescope with a relatively higher cadence. All the PTF/iPTF light curves are stored in the NASA/IPAC infrared science archive[15]

ZTF[16] is a new robotic time-domain survey on the P48 telescope mounted on a new 600 megapixel camera with a 47 deg^2 field of view (Bellm et al. 2019). It covers the entire visible northern sky (decl. $>-30°$) from 2018 to present. ZTF's extremely wide field and fast readout electronics enables a survey that scans more than 3750 deg^2 per hour, to a 5σ detection limit of $g \sim 20.8$ and $r \sim 20.6$ mag (AB system) with a 30 s exposure during new moon (Masci et al. 2019). The ZTF data are aperture-based photometry with a typical aperture diameter of 2″. The data can be accessed via ZTF commands[17].

2.4. Pan-STARRS

The Panoramic Survey Telescope & Rapid Response System (Pan-STARRS or PS1; Chambers et al. 2016) covers 30,000 deg^2 of the sky north of decl. $>-30°$ from 2010 to 2016 using a 1.8 m telescope in Hawaii, with typically ∼12 epochs for each filter (*grizy*). The mean 5σ point-source limiting sensitivities in a single-epoch exposure of *grizy* are 22.0, 21.8, 21.5, 20.9, 19.7 AB magnitude, respectively. All the detections are obtained via the Pan-STARRS Catalog Search interface.[18]

2.5. DECaLS

The Dark Energy Camera Legacy Survey (DECaLS) aims to provide the optical imaging for target selection in the DESI survey, covering ∼9000 deg^2 both the North Galactic Cap region at decl. $\leqslant 32°$ and the South Galactic Cap region at dec $\leqslant 34°$ (Dey et al. 2019). The 5σ depths in final stacked *grz* band images are 24.0, 23.4, and 22.5 AB magnitude. The single-epoch exposure is from the forced photometry with different aperture sizes. All the data are obtained from the data lab in NOAO[19] combining three tables (i.e., ls_dr8.tractor, ls_dr8.ccds_annotated, and ls_dr8.forced).

2.6. Photometric Data Calibration

To verify the CL behavior with photometric evidence from different surveys, we compile the light curve for each candidate in the r band, which usually has the best filter transmission and/or S/N with sufficient photometries. We convert all magnitudes to the AB system. Then, we correct the differences between various filter systems to calibrate the magnitudes to the same scale, though the deviations are very small (corrections to SDSS$-r$ for CRTS$-V$, PTF/iPTF$-R$, ZTF $-r$, PS1$-r$, and DECaLs$-r$ are -0.115, -0.102, -0.034, -0.002, and -0.035 AB mag, respectively). We have adopted the aperture-based (∼2″) photometries from all surveys. The synthetic magnitudes of the SDSS spectra are obtain by convolving the spectrum with SDSS$-r$ filter with `PySynphot`[20] (STScI Development Team 2013).

Table 1
EVQs Selection from SDSS DR16 Repeat Spectra

Selection	Spectra	Objects
Parent sample	5,789,200	...
(1) Class="QSO" or "GALAXY"	...	...
(2) Nepoch ⩾2 and zWarning=0	748,769	313,877
(3) Redshift: $1.5 < z < 4.9$	237,958	92,422
(4) $S/N_{1450} > 3$ and $S/N_{CIV} > 5$	129,877	61,037
(5) $Flux_{1450}$: (MAX-MIN)/MEAN >1	5,474	1,039
(6) Reject SDSS-RM objects	1818(+4041 recycled)	951
(7) Require spectral change or variability confirmed by light curves	638(+451 recycled)	348
(8) CLQ: any prominent broad-UV-line flux is consistent with zero	27(+32 recycled)	23

Note. The recycled objects denote the low-S/N EVQs removed by Criterion 4. In (8), the broad UV line refers to any of Ly α, Si IV, C IV, C III], or Mg II.

3. Sample Selection

3.1. Preliminary Screening

Our strategy is using repeat spectra in SDSS to search for high-redshift EVQs/CLQs. We first select the EVQ/CLQ candidates from the whole SDSS spectroscopic database via Criteria 1–6 in Table 1. Then, we remove spurious EVQs/CLQs by visual inspection due to problematic flux calibration of SDSS spectra with assessments from the concurrent multisurvey photometries and spectral variation (Criterion 7; see the details in Section 3.3). Finally, we separate CLQs and normal EVQs with Criterion 8. In this section, we describe this selection procedure in detail.

We start with all spectra (5.8 million) in the SDSS DR16 database (Ahumada et al. 2020), which was released in 2019 December. Criteria 1 and 2 are applied to guarantee that repeat quiescent/active galaxy observations are not subject to the problematic redshifts. The target classification and redshift measurements are obtained via the software `REDMONSTER`[21] (Hutchinson et al. 2016). This yields a repeat spectral catalog archived on Zenodo (doi:10.5281/zenodo.3892020), which contains 313,877 multiepoch quiescent/active galaxies. This catalog includes basic continuum and line measurements based on the SDSS pipeline (Bolton et al. 2012). In addition to CLQ searches, this repeat catalog is also useful for other scientific goals, e.g., post-TDE candidates with strong variability of their broad nitrogen line (Liu et al. 2018; Jiang et al. 2008), studies of continuum and emission-line variability (Wilhite et al. 2005; Guo & Gu 2014, 2016; Ruan et al. 2014), identifying supermassive BH binary candidates with the radial velocity shift of the broad emission lines (Eracleous et al. 2012; Liu et al. 2014; Runnoe et al. 2017; Guo et al. 2019).

[15] https://irsa.ipac.caltech.edu/Missions/ptf.html
[16] https://irsa.ipac.caltech.edu/Missions/ztf.html
[17] https://www.ztf.caltech.edu/page/dr2#12b.iii
[18] https://catalogs.mast.stsci.edu/panstarrs/
[19] https://datalab.noao.edu/query.php
[20] https://pysynphot.readthedocs.io/en/latest/
[21] https://github.com/timahutchinson/redmonster

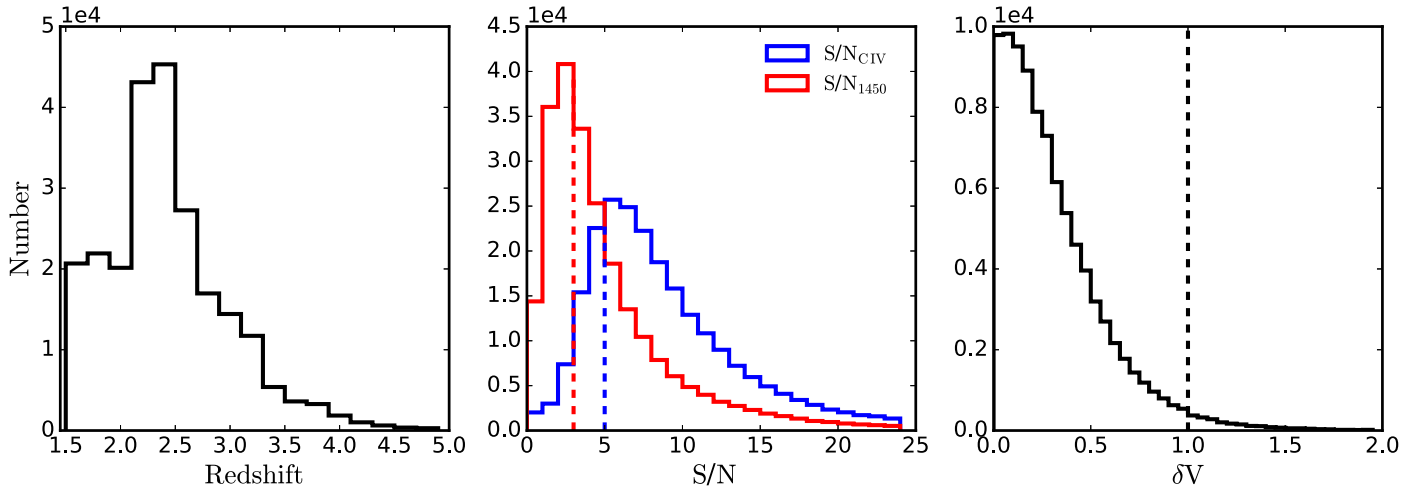

Figure 1. Left: the redshift distribution for 237,958 objects (92,422 objects) ranging from $z = 1.5$ to 4.9 with a peak around $z = 2.2$. Middle: distributions of the median S/N per pixel for the continuum at 1450 Å (red) and C IV line (blue). The red/blue dashed lines present the different S/N cuts (i.e., S/N$_{1450} > 3$ and S/N$_{CIV} > 5$). Right: distribution of continuum variability at 1450 Å for 92,422 objects. Criterion 4 selects EVQ objects with $\delta V \equiv \frac{\mathrm{Max}-\mathrm{Min}}{0.5(\mathrm{Max}+\mathrm{Min})} > 1$.

In order to discover CLQs with prominent UV lines (e.g., C IV) and estimate the BH mass at high redshift, Criterion 3 is set to ensure the C IV line is in the SDSS wavelength coverage. The redshift distribution is shown in Figure 1 (left panel), whose peak is around 2.2 (a feature designed by the baryon oscillation spectroscopic survey to map the large-scale structure traced by the Lyα forest). We measure the S/N of the C IV line in [1500,1600] Å and a line-free continuum window [1450, 1460] Å for those spectra that satisfy criteria 1–3. Figure 1 (middle panel) presents the S/N distributions of continuum around 1450 Å and C IV line. We cut the S/N$_{CIV} > 5$ and S/N$_{1450} > 3$ for emission-line and continuum S/Ns (Criterion 4).

Previous investigations (e.g., Yang et al. 2018) indicate that CLQs presenting the appearance/disappearance of broad emission lines are always accompanied by continuum variations, although sometimes the variation is tiny. Criterion 5 requires the continuum variability at 1450 Å, $\delta V \equiv \frac{\mathrm{Max}-\mathrm{Min}}{\mathrm{Mean}} > 1$, where $\mathrm{Mean} = \frac{1}{2}(\mathrm{Max} + \mathrm{Min})$. This is equivalent to Max/Min >3, approximately consistent with previous EVQ/CLQ selection ($|\Delta g| > 1$ mag) in other works (MacLeod et al. 2016; Rumbaugh et al. 2018) considering the median redshift is around 2.2 in our sample. Note that the average number of repeat observations for each object after this criterion rapidly increases to 5 from 2, indicating that many other EVQs were not selected, probably due to the lack of frequent observations. The distribution of continuum variability is also plotted in Figure 3 (right panel), which rejects ∼98% objects with little/mild variability. This variability cut may miss some CLQs with tiny continuum variation (e.g., the Mg II CLQ with variability of 0.1 mag in the r band; Guo et al. 2019). Criterion 6 removes all the objects in the SDSS-RM program (centered at R.A. = 213.704, decl. = +53.083 with a field of view of 7 deg^2) as only a low-redshift CLQ was discovered in the SDSS-RM sample (Wang et al. 2018; Dexter & Begelman 2019), and more careful analysis could be conducted for SDSS-RM EVQs with extensive spectroscopies and simultaneous photometries over 6 yr (Shen et al. 2015).

Finally, we are left with 951 EVQ objects with 1818 spectra (also see Table 1). For these 951 objects, we recycle every epoch rejected in Criterion 4 due to the low spectral S/N, because these low-S/N epochs are likely to be the faint states of real CLQs experiencing large continuum variations. The S/N cut ensures that at least one epoch in an object meets the S/N criterion for BH mass measurement.

3.2. Spectral Flux-calibration Problem

In Appendix A.1, we demonstrate that SDSS high-redshift quasar spectra are subject to an intrinsic flux-calibration scatter of ∼20%. The variability criterion ($\delta V > 1$) is much larger than the intrinsic calibration scatter, which should have less influence on our EVQ/CLQ selection. We also describe the fiber-drop issue in Appendix A.2, which leads to a significant reduction of the spectral flux. Epochs suffering from fiber drop with a huge flux reduction can mimic EVQs/CLQs (see Figure A2). Therefore, cross-identification, e.g., with concurrent photometries, is crucial for robust EVQ/CLQ selection.

3.3. Visual Inspection for EVQs/CLQs

We then visually inspect the brightest and faintest epochs to screen for real EVQs/CLQs following these rules: (1) objects with significant spectral changes, e.g., spectral slope or emission-/absorption-line profiles (2) or the spectral synthetic magnitude of the faintest epoch is consistent with the nearest multisurvey photometric/synthetic magnitudes (e.g., within a window of ± 1 yr). The brightest spectrum in each object is usually consistent with the concurrent photometries and barely affected by the fiber-drop problem. Also, we checked that multisurvey photometries are still reliable even when they exceed the 5σ limiting magnitude (e.g., CRTS photometries fainter than 21 mag are still broadly consistent with SDSS spectrophotometry). This selection may miss some real EVQs/CLQs with neither concurrent photometries nor obvious spectral variation (uncertain epochs). However, our selection is not pursuing the completeness of EVQs/CLQs at high redshift, but rather a pure sample to investigate their physical properties. In total, these two rules effectively reject ∼10% of fiber-loose objects and ∼50% of uncertain epochs. In addition, we also eliminate <5% of problematic spectra due to lack of data or strong telluric-line residuals.

This leaves 348 significant EVQs. Then, we use the spectral decomposition technique to measure the continuum/emission-line properties (see Section 3.4). As suggested, CLQs are likely to be a

part of the EVQ tail of normal quasars and EVQs are good candidates to search for CLQs (Rumbaugh et al. 2018). However, the definition of a CLQ is pretty ambiguous and arbitrary, as well as strongly dependent on the spectral S/N (Guo et al. 2020; also see Section 5.3). Therefore, we here adopt a temporary definition[22] of CLQ, analogous to what has been done at low redshift, to explore the properties of high-redshift CLQs. We quantitatively define CLQs as those whose faint-epoch line flux (at least one prominent broad UV line, i.e., Ly α, Si IV, C IV, C III], Mg II) is consistent with zero within its uncertainty ($flux < 3\sigma$). This yields 23 CLQs showing broad-line appearance/disappearance or are very close to completing this transition as shown in Figures 2 and B1–B3. In total, our sample includes 1 C IV, 19 C III], 16 Si IV, and 4 Mg II CLQs, with some individual objects showing CL behavior in more than one line. Note that we also occasionally discover an obvious C II] CLQ in Figure B1.

The broad-line component in CLQs usually gradually transitions from a strong broad emission line to a weak one easily swamped by noise, and finally to an absorption line with the continuum decreasing continuously. Figure 2 exhibits six randomly selected examples of high-redshift CLQs with changes in different lines. In each panel, we present the brightest and faintest epochs (middle panel), spectral ratio (bottom panel), and r-band light curve (top panel). Most objects present the typical bluer-when-brighter (BWB) trend (i.e., the quasar continuum becomes bluer when it gets brighter; Sun et al. 2014; Guo & Gu 2016; Cai et al. 2019), accompanied by at least one transitioning line. The CL behavior is confirmed either by spectral change (see spectral ratio) or concurrent photometries in the g-band light curve. The weak UV emission lines (e.g., 19 C III], 16 Si IV, and 4 Mg II CLQs) are usually easier to change than the strong lines, for instance, C IV (only ID = 112340 in Figure 2 if not very clean) and Lyα (no Lyα CLQ). During the transitions, the line core component is usually more variable than the line wings, e.g., the line core of C III] in ID = 23445 in Figure B1 has transferred into an absorption line while the line wing is still persistent, which is consistent with the photoionization model.

3.4. Spectral Fitting

To determine the variability properties of the broad emission lines and to measure their profiles for virial BH mass estimates, we fit spectral models following Shen et al. (2019) using the software `PyQSOFit` (Guo et al. 2018). The model is a linear combination of a power-law continuum, a third-order polynomial (to account for reddening), a pseudo-continuum constructed from UV/optical Fe II emission templates, and single or multiple Gaussians for the emission lines. We do not include a host galaxy component because such a component is negligible for quasars at $z > 1.5$. The Balmer continuum is also not included due to its major contribution being in ~3000–3600 Å, which exceeds our wavelength coverage.

We adopt a global fit to model the relatively emission-line-free region to quantify the continuum. We then fit multiple Gaussian models to the continuum-subtracted spectrum on individual line complexes. Table 2 lists the detailed information of line complexes and the fitting parameters. In each line complex, we simultaneously fit a set of Gaussians to individual lines with a boundary of 1200 km s^{-1} to separate broad and narrow components. The measurement uncertainties of the spectral properties (e.g., continuum luminosity, line width, etc.) are estimated with a Monte Carlo approach by repeatedly fitting the spectrum for 50 trials perturbed with a zero-mean random Gaussian noise whose σ is the original error in each pixel. All of the related measurements are saved in our EVQ catalog (see Section 3.5 and Table 3).

Because high-redshift quasars are potentially subject to broad/narrow absorption lines that may bias the continuum and emission-line fits, we perform the following steps to amend this effect: (1) mask pixels that are 3σ below the SDSS built-in model, which is constructed by a principal component analysis using quasar/galaxy templates with `REDMONSTER`; (2) perform one iteration for the continuum fit to reject pixels that fall 3σ below the previous fit; and (3) reject pixels in emission-line regions that fall 3σ below the continuum model for the emission-line fitting. The combination of these criteria significantly alleviates measurement bias from narrow/broad absorption lines.

3.5. The EVQ Catalog

We have tabulated the measured quantities of 348 EVQs including 23 CLQs from the spectral fitting in the online catalog of this paper, and the catalog format is listed in Table 3. Below we describe the specifics of the cataloged quantities.

1. Object ID: the repeat catalog index of SDSS DR16.
2. Spectroscopic plate ID, Modified Julian Date (MJD) and fiber ID: the combination of plate–MJD–fiber locates a particular spectroscopic observation in SDSS.
3. R.A., decl. (in J2000.0), and redshift. All of the spectra are flagged with zWarning = 0, indicating a good quality of the spectroscopic redshift measurement.
4. Nepoch: number of repeat spectroscopic observations.
5. FIRST detection: if there is a source in the FIRST radio catalog (version 2014 December) within 2.″0 of the quasar position, 1 if detected in FIRST; 0 if not; −1 if the quasar lies outside of the FIRST footprint.
6. FIRST peak flux density: observed flux in 20 cm; −1 = not in FIRST footprint; 0 = FIRST undetected.
7. Flag: 1 = brightest epoch; −1 = faintest epoch.
8. δV: the continuum variability at 1450 Å; $\delta V \equiv \frac{\mathrm{Max}-\mathrm{Min}}{0.5(\mathrm{Max}+\mathrm{Min})}$.
9. f_{1450}: observed flux in rest frame at 1450 Å without corrections of the intrinsic extinction/reddening.
10. S/N_{1450} and S/N_{CIV}: the median S/N per pixel in continuum region [1425, 1475] Å and C IV emission-line region [1500,1600] Å.
11. Continuum luminosity and uncertainties at 1350 Å.
12. Line FWHM, rest-frame EW, and their uncertainties for C IV; −1 if not available.
13. Virial BH masses and uncertainties using calibrations of C IV (VP06); −1 if not available.
14. Average virial BH masses and uncertainties of the brightest and faintest epochs. If only brightest epoch is available, we use $M_{\mathrm{BH,Mean}} = M_{\mathrm{BH,Bright}} - 0.15$ dex, otherwise, $M_{\mathrm{BH,Mean}} = M_{\mathrm{BH,Faint}} + 0.15$ dex to mitigate the BH mass discrepancy of 0.3 dex in bright/faint states.
15. Eddington ratio: based on the mean virial BH mass.
16. The reduced χ^2_ν for the C IV fitting in [1500, 1700] Å.
17. Type: 0 = CLQ; 1 = EVQ.

[22] Because we eventually find that CLQs and EVQs are the same population, we recommend using EVQ to refer to the entire extremely variable quasar population.

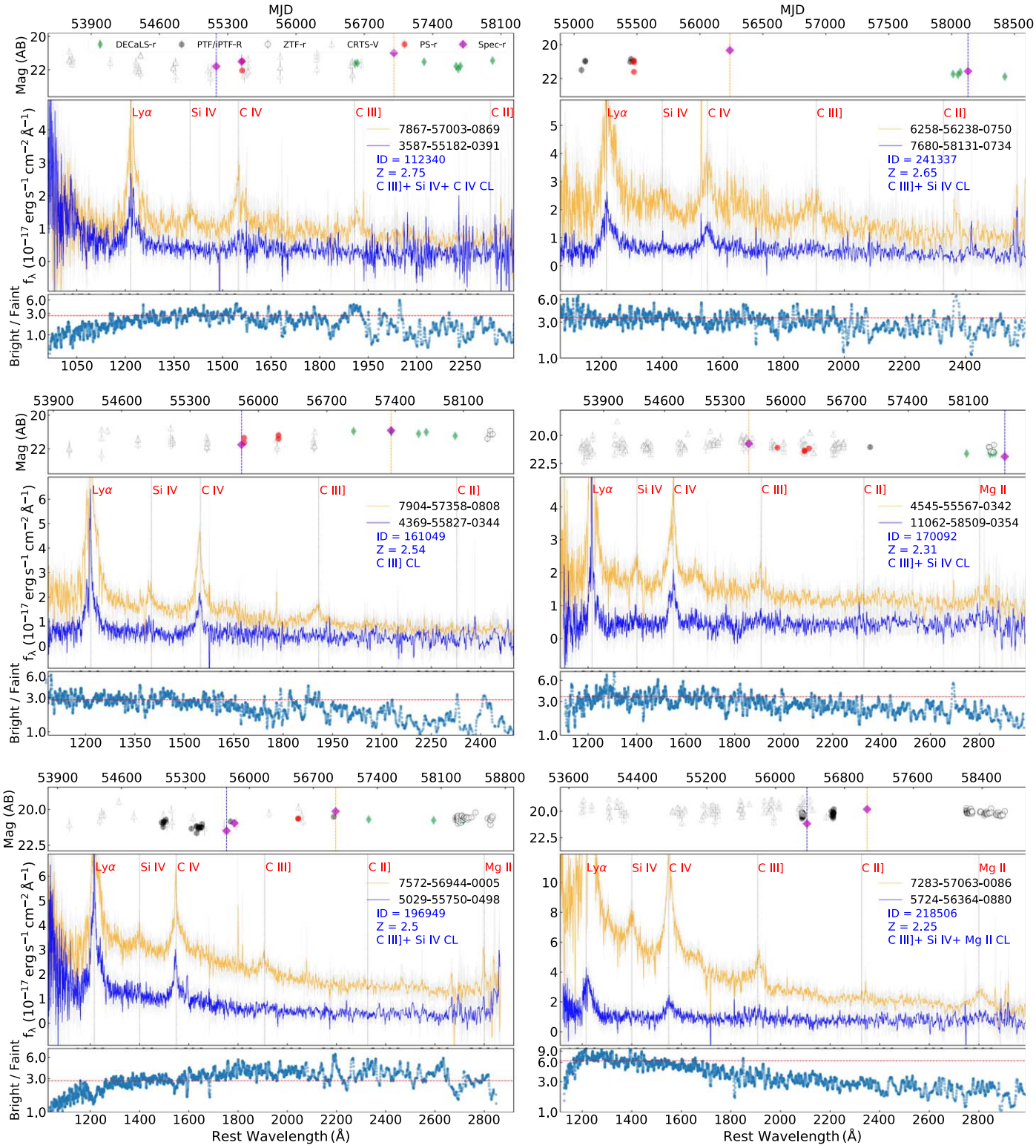

Figure 2. Examples of CLQs. We demonstrate six out of 23 CLQs showing transitions in different lines (listed in blue text). The rest are shown in Appendix B. Each panel presents the brightest and faintest epochs (middle), *r*-band multisurvey light curve corrected for the difference among photometric systems (top), and the spectral ratio between the bright and faint epochs in each object (bottom). All of the spectra are smoothed with a boxcar of 5 pixels for clarity, except the original SDSS spectra (light gray). The red line in the bottom panel is the flux ratio at 1450 Å to guide the eye.

4. EVQ/CLQ Properties

Rumbaugh et al. (2018) and Luo et al. (2020) have extensively explored the distinctions between EVQs and normal quasars with light curves over ∼16 yr and suggested that EVQs seem to be in the tail of a continuous distribution of quasar properties, rather than standing out as a distinct population. One of our main purposes for this work is to further examine the possible difference between the EVQs and CLQs, although with a relatively smaller (but currently the

Table 2
Line Fitting Parameters

Line Complex (1)	Fitting Range [Å] (2)	Line (3)	$n_{\rm gauss}$ (4)
Si IV	1290–1450	Broad Si IV/O IV]	2
		C II 1335	1
		O I 1304	1
C IV	1500–1700	Broad C IV	3
		Broad He II 1640	1
		Narrow He II 1640	1
		Broad O III 1663	1
		Narrow O III 1663	1
C III]	1700–1970	Broad C III]	2
		Si III] 1892	1
		Al III 1857	1
		[Si II] 1816	1
		[N III] 1750	1
		[N IV] 1718	1
Mg II	2700–2900	Broad Mg II	2
		Narrow Mg II	1

Table 3
FITS Catalog Format

Column	Format	Description
1…	LONG	Object ID in repeat DR16 catalog
2…	LONG	Spectroscopic plate number
3…	LONG	MJD of spectroscopic observation
4…	LONG	Spectroscopic fiber number
5…	DOUBLE	Right ascension in decimal degrees (J2000.0)
6…	DOUBLE	decl. in decimal degrees (J2000.0)
7…	DOUBLE	Redshift
8…	LONG	Number of spectroscopic observations
9…	LONG	First detection: detected = 1; not detected = 0; out of FIRST footprint = −1
10…	DOUBLE	Observed FIRST flux density at 20 cm [mJy]
11…	LONG	Flag represents the brightest (1) and faintest epochs (−1) in an object
12…	DOUBLE	Rest frame continuum variability at 1450 Å, $\delta V \equiv \frac{\rm Max-Min}{0.5({\rm Max+Min})}$
13…	DOUBLE	Observed optical flux density at rest frame 1450 Å [ergs cm^{-2} s^{-1} Å^{-1}]
14…	DOUBLE	Signal-to-noise ratio of continuum around 1450 Å
15…	DOUBLE	Signal-to-noise ratio of C IV line
16…	DOUBLE	Monochromatic luminosity at 1350 Å [$\log(L_{1350}/{\rm ergs^{-1}})$]
17…	DOUBLE	Uncertainty in $\log L_{1350}$
18…	DOUBLE	FWHM of the whole C IV [km s^{-1}]
19…	DOUBLE	Uncertainty in C IV FWHM
20…	DOUBLE	Rest-frame equivalent width of the broad C IV [Å]
21…	DOUBLE	Uncertainty in $\rm EW_{CIV}$
22…	DOUBLE	Virial BH mass based on C IV [VP06, $\log(M_{\rm BH,vir}/M_\odot)$]
23…	DOUBLE	Measurement uncertainty in $\log M_{\rm BH,vir}$ (C IV, VP06)
24…	DOUBLE	The adopted fiducial virial BH mass: $M_{\rm BH} = \frac{1}{2}(M_{\rm bright} + M_{\rm faint})$ [$\log(M_{\rm BH,vir}/M_\odot)$]
25…	DOUBLE	Uncertainty in the fiducial virial BH mass (measurement uncertainty only)
26…	DOUBLE	Eddington ratio based on the fiducial virial BH mass
27…	DOUBLE	Reduced χ^2 for the C IV line fitting
28…	LONG	Type = 0 if CLQs, otherwise type = 1 for EVQs

(This table is available in its entirety in machine-readable form.)

largest) sample size of high-redshift CLQs. Note that we use EVQ to denote the non-CL EVQs in the following sections.

4.1. Basic Properties

A sample of 348 EVQs are selected through repeat observations in SDSS with $\delta V > 1$. As shown in the first two panels of Figure 3, most EVQs/CLQs concentrate upon a number of epoch less than 5. We found 140 (6) EVQs (CLQs) brightened and 185 (17) EVQs (CLQs) dimmed. The last panel shows the distribution of the rest-frame time separations between the brightest and faintest epochs of each EVQ/CLQ. The short-term large variability is intrinsically rare, such that only a few objects with time separation less than 100 days are observed. The drop of objects beyond ∼1000 days (∼3000 days in observed frame considering a median redshift of 2.2) is largely due to the quasar selection bias before DR9 (2010), which primarily selected quasars with $z < 2$, rather than a real rarity of EVQs at these timescales. All the CLQs are distributed in a range of ∼100–900 days in the rest frame.

Out of 348 EVQs, 319 are within the Faint Images of the Radio Sky at Twenty-centimeters (FIRST) coverage, and 9 of them are radio detected, resulting in a radio fraction of ∼3%, which is consistent with previous results that the radio fraction of quasars will gradually decrease (e.g., <5% at $z > 1$) with increasing redshift and decreasing luminosity (Jiang et al. 2007).

4.2. Emission-line Properties

The spectral fitting technique is used to decompose the brightest and faintest spectra of 348 EVQs/CLQs, as described above in Section 3.4. Measurements of Si IV, C III], and Mg II are not as accurate as C IV due to their weaker intensity or even disappearing in some CLQs. In addition, Mg II always very closely approaches or exceeds the long-wavelength edge, leading to only about half of our objects having reliable Mg II spectral measurements. Therefore, we focus on the measurements based on C IV in the following sections, and related measurements are listed in the EVQ catalog (Table 3).

4.2.1. δV, L_{1350}, EW, and FWHM

Figure 4 presents the distributions of continuum variability at rest frame 1450 Å, continuum luminosity at rest frame 1350 Å, equivalent width (EW), and FWHM of the broad component of C IV. The corresponding means and uncertainties are listed in Table 4. The continuum variabilities δV of EVQs/CLQs show no significant difference considering the errors, and the CLQs are not biased to the largest variability end. As expected, the average L_{1350} (i.e., $10^{45.78}$ and $10^{45.27}$ erg s^{-1} for the bright and faint states) are much fainter than that of the normal high-redshift quasars (i.e., ∼46.15 erg s^{-1}) in DR 7 (Shen et al. 2011), given the anticorrelation between the Eddington ratio and variability (e.g., Guo & Gu 2016; Rumbaugh et al. 2018). The average difference of 0.5 dex between bright and faint states is consistent with our variability criterion (i.e., continuum flux at 1450 Å: Max/Min > 3). The largest variability in our sample reaches ∼1 dex in SDSS baseline over ∼18 yr. The C IV EW distributions of bright and faint states of EVQs are also well separated by ∼0.3 dex. According to the well-known Baldwin effect (Baldwin 1977), $L_{\rm con} \propto 1/{\rm EW}$, fainter EVQs exhibit higher emission-line EWs, consistent with the C IV result in the second panel. The

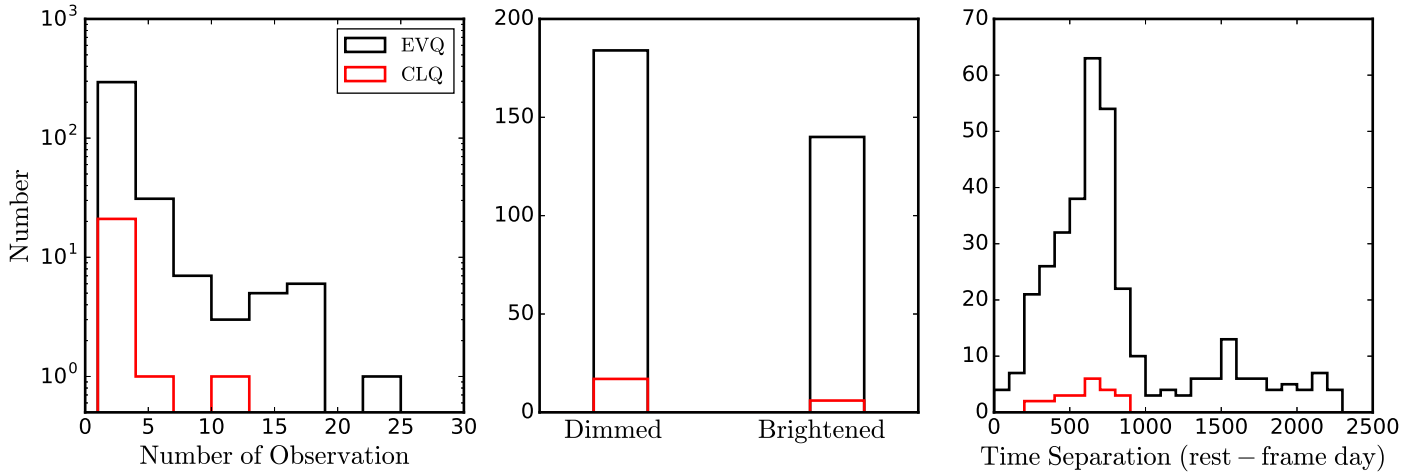

Figure 3. Distributions of number of observation, brightened and dimmed objects, and maximum time separation in the rest frame for EVQs/CLQs. Black and red lines represent EVQs and CLQs, respectively.

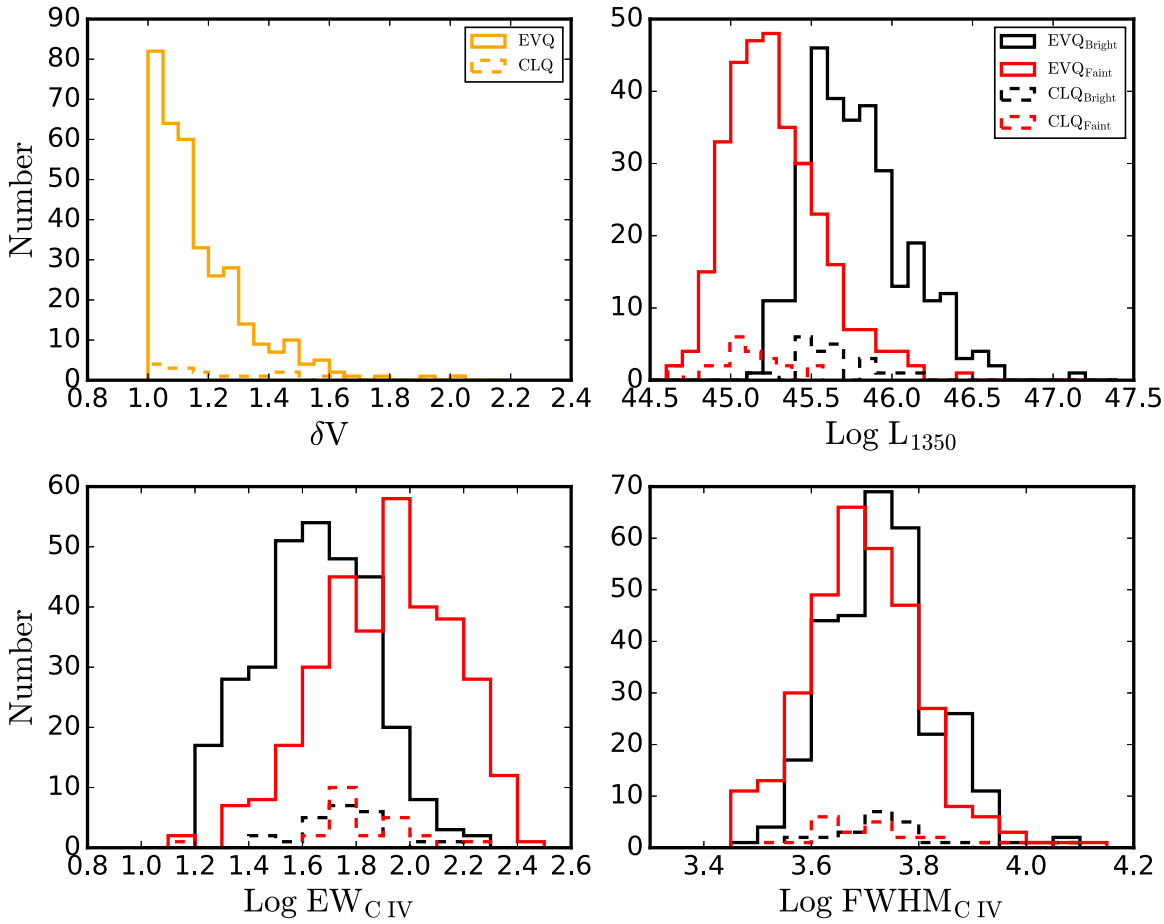

Figure 4. Distributions of continuum luminosity at 1350 Å, EW, and FWHM of C IV. Black and red solid (dashed) lines denote the bright and faint states of EVQs (CLQs). Their mean values and the same-state K-S test results are listed in Table 4, respectively.

third panel shows that the FWHM distribution for the faint EVQs is on average slightly lower than that of the bright EVQs. This is the opposite of what the breathing model predicts: $L_{\rm con} \propto 1/{\rm FWHM}$, discovered in Balmer lines (e.g., Cackett & Horne 2006; Denney et al. 2009; Barth et al. 2015; Wang et al. 2020). However, the antibreathing of C IV is not newly discovered and has been reported in previous investigations (e.g., Wills et al. 1993; Wilhite et al. 2006; Denney 2012; Shen 2013; Guo & Gu 2016; Wang et al. 2020). The origin of this antibreathing phenomenon is likely due to the existing of a nonreverberating component in C IV, which may originate from the intermediate-line region (between the broad and narrow emitting regions with FWHM ∼1200–2000 km s^{-1}) or an outflow (see details in Sections 4.3 and 5.5).

Table 4
EVQ and CLQ Properties

	EVQ	CLQ	EVQ	CLQ	K-S Test between EVQs and CLQs	
	Bright State		Faint State		Bright State	Faint State
δV	1.17 ± 0.16	1.27 ± 0.24	1.17 ± 0.16	1.27 ± 0.24	6.4×10^{-2}	6.4×10^{-2}
$\mathrm{LogL_{1350}}$ (erg $\mathrm{s^{-1}}$)	45.78 ± 0.31	45.62 ± 0.21	45.27 ± 0.29	45.08 ± 0.22	1.5×10^{-2}	5.3×10^{-3}
$\mathrm{EW_{CIV}}$ (Å)	50 ± 26	62 ± 26	94 ± 50	73 ± 32	5.5×10^{-3}	5.2×10^{-2}
$\mathrm{FWHM_{CIV}}$ (km $\mathrm{s^{-1}}$)	5522 ± 1322	5813 ± 1591	5144 ± 1349	5614 ± 1975	5.2×10^{-2}	8.3×10^{-1}
$\mathrm{Log}\lambda_{\mathrm{Edd}}$	−0.64 ± 0.23	−0.76 ± 0.23	−1.11 ± 0.24	−1.30 ± 0.25	1.2×10^{-2}	3.6×10^{-2}

4.2.2. A Nonreverberating Component in C IV

Figure 5 presents a clear example of an EVQ with a nonreverberating component, leading to the C IV antibreathing phenomenon (e.g., Wang et al. 2020). C IV consists of a very broad component (red; FWHM = 12,300 km $\mathrm{s^{-1}}$) and an intermediate broad component (IBC, green; FWHM = 1900 km $\mathrm{s^{-1}}$) in the bright state, while the very broad component has disappeared in the faint state, resulting in the total FWHM being significantly reduced (i.e., 2250–1900 km $\mathrm{s^{-1}}$; anti-breathing). Note that the broad green component in the faint epoch is tied to that in the bright state assuming this IBC is constant. The goodness of fit with $\chi^2_\nu = 2.6$ in the faint spectrum indicates the IBC indeed does not change too much even as an EVQ. If one considers the IBC as a "narrow" component in C IV, it could be classified as a generalized CLQ according to the traditional definition.

4.2.3. Same-state Comparison between CLQs and EVQs

Comparing the same-state property distributions of EVQs and CLQs in Figure 4 with Kolmogorov–Smirnov (K-S) test, we find that most p values of the luminosity, EW, and FWHM are not smaller than 0.01 in Table 4; that is, at a significance level of 0.01, we cannot reject the null hypothesis that EVQs and CLQs are drawn from the same continuous distribution. On the other hand, the same-state CLQs on average present similar but slightly lower continuum luminosity and broader FWHM in Table 4, which hint at possible lower Eddington ratios for CLQs. However, those slight differences are still much smaller than the uncertainties. We therefore suggest that there is no strong evidence that EVQs and CLQs are different in these various properties, supporting that CLQs are likely to be a subset of EVQs.

4.3. BH Mass

We estimate the AGN BH mass using the single-epoch estimator assuming virialized motion in the BLR clouds (Shen 2013). With the continuum luminosity as a proxy for the BLR radius and the broad emission-line width, characterized by the FHWM, as an indicator of the virial velocity, the virial mass estimate can be expressed as

$$\log\left(\frac{M_{\mathrm{BH}}}{M_\odot}\right) = a + b\log\left(\frac{\lambda L_\lambda}{10^{44}\ \mathrm{erg\ s^{-1}}}\right) + 2\log\left(\frac{\mathrm{FWHM}}{\mathrm{km\ s^{-1}}}\right), \quad (1)$$

where $L_\lambda = L_{1350}$ for C IV. The coefficients a and b are empirically calibrated based on the local reverberation-mapped AGNs and scaling relations between UV and optical lines. We adopt the calibrations of Vestergaard & Peterson (2006) (VP06) with $a = 0.66$ and $b = 0.53$ for the C IV line.

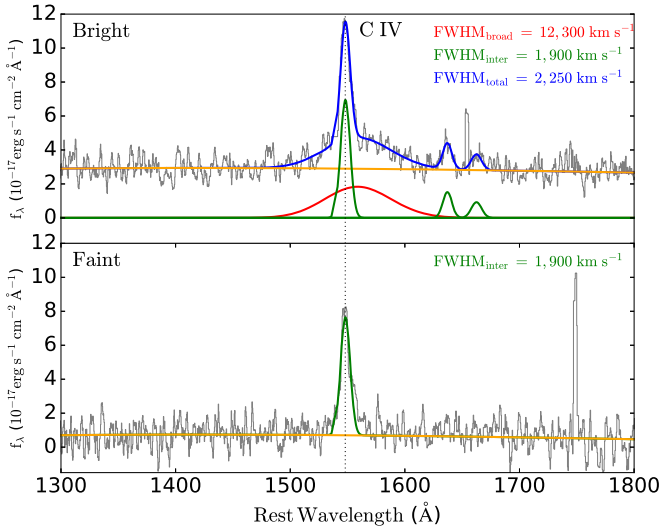

Figure 5. Example of an antibreathing C IV (SDSS J225519.57−010009.4). The broad red component (FWHM = 12,300 km $\mathrm{s^{-1}}$) has disappeared as its continuum decreased within 2.1 yr in the rest frame, indicating a positive correlation between L_{con} and $\mathrm{FWHM_{C\ IV}}$ (i.e., antibreathing). The bright state is best fitted with four Gaussian profiles (two for C IV, and one each for He II 1640 Å and O III 1663 Å), while the width of all the green Gaussian profiles in both the bright and faint states are tied together.

According to the photoionization model (Goad et al. 1993; Baldwin et al. 1995; Korista & Goad 2000; Guo et al. 2020), the observed broad-line flux is actually dominated by the BLR clouds in a relatively narrow ring assuming a disk-like BLR (Gravity Collaboration et al. 2018), where the clouds are best able to reprocess the incident continuum. The average cloud distance to the center will increase when the continuum luminosity increases, yielding a slower rotational velocity of the clouds (FWHM), namely the broad-line breathing model. However, the C IV FWHM increases when the quasar brightens in Figure 4, which presents an opposite behavior.

This antibreathing behavior of C IV in Figure 4 will result in a serious problem: luminosity-dependent BH mass (i.e., higher BH mass with increasing continuum luminosity; Shen 2013). Figure 6 presents the BH masses measured in the brightest/faintest states for each EVQ/CLQ. The best linear fit of the EVQ sample is significantly offset from a one-to-one relation, with an average difference of ∼0.3 dex between the bright and faint BH masses. CLQs are randomly distributed in EVQs without any obvious difference, except the outlier with the highest faint-state BH mass, which is a C IV CLQ (ID = 112340). We simply adopt the average as our fiducial

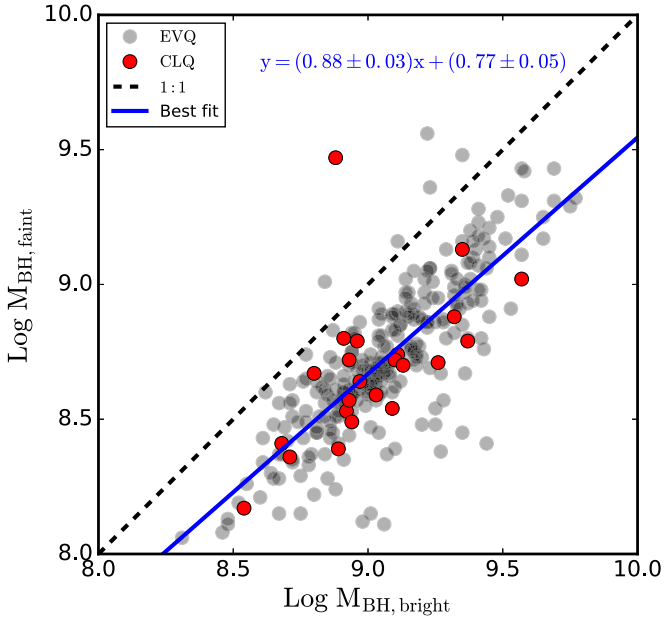

Figure 6. Discrepancy of BH masses in bright and faint states. The blue line is the best linear fit for the EVQ+CLQ sample and the coefficient errors are estimated with the bootstrap method. The antibreathing behavior in C IV results in a ∼0.3 dex offset relative to the 1:1 BH mass ratio. The red outlier with the highest faint-state BH mass is a C IV CLQ (ID = 112340).

BH mass, because there is still no ideal solution for this issue to date (see discussion in Section Section 5.5). However, we caution that this BH mass will suffer an extra scatter (0.3 dex) introduced by quasar variability.

4.4. Eddington Ratio

With the continuum luminosities at 1350 Å derived from the spectral fitting for the bright and faint states, we can estimate the bolometric luminosity with $L_{\rm bol} = 3.81 L_{1350}$ according to Richards et al. (2006), hence the Eddington ratio $\lambda_{\rm Edd} = L_{\rm bol}/L_{\rm Edd}$, where $L_{\rm Edd} = 1.26 \times 10^{38} M_{\rm BH,Mean}/M_{\odot}$ erg s^{-1} based on the averaged BH mass.

Extensive investigations have demonstrated an anticorrelation between variability and Eddington ratio in normal quasars (e.g., Wilhite et al. 2008; Ai et al. 2010; MacLeod et al. 2010; Guo & Gu 2014), and Rumbaugh et al. (2018) exhibit this negative relation further, extending to EVQs with ∼1000 photometrically selected quasars. Figure 7 also confirms this relation between the $M_{\rm BH,Mean}$-based Eddington ratio and maximum spectral variation at 1450 Å, especially in the faint state. The most striking feature is that the average Eddington ratio of CLQs is lower than that of EVQs, particularly in the faint state (∼0.2 dex) but only with a confidence level of $\lesssim 1\sigma$. Actually, this feature is implicitly inferred by their slightly lower luminosity and broader FWHM relative to the normal EVQs in Table 4 and Figure 4. However, the sample size of CLQs is still not large enough, and the bolometric correction may be different when the spectral energy distribution changes. Furthermore, the uncertainty of the Eddington ratio for individual objects is quite large due to the intrinsic BH mass uncertainty (∼0.4 dex, Shen 2013) and the extra variability-induced scatter (∼0.3 dex) in Section 4.3. Therefore, we suggest that the evidence here is not conclusive enough to prove that CLQs are a subset of EVQs with less efficient accretion.

Table 4 shows the same-state comparison between CLQs and EVQs with the K-S test. The p values of the maximum variability and Eddington ratio are not all smaller than 0.01, which indicates that we cannot reject the null hypothesis at the 0.01 significance level. This is generally consistent with the K-S results of the continuum luminosity, EW, and FWHM, further supporting that CLQs and EVQs are likely to be the same population.

We also distinguish different CLQs with different circles in Figure 7. The majority of CL behaviors are C III] and Si IV CLQs, primarily due to their relatively weak line intensity (see the details in Section 5.1). In addition, the critical Eddington ratio for the state transition of UV lines seems to be around 0.01 to 0.1, and the critical $\lambda_{\rm Edd}$ for C III] and Si IV is definitely higher than C IV and Ly α, as the broad C IV and Lyα are still persistent in almost all EVQs. C II] CL behavior is not common in our sample and most C II] lines have already disappeared in bright state of C III] CLQs due to its low luminosity, easily swamped by spectral noise. Therefore, we suggest that the critical Eddington ratio of the CL behavior in different lines basically follows $\lambda_{\rm Edd,C\ II]} > \lambda_{\rm Edd,Si\ IV,C\ III],Mg\ II} > \lambda_{\rm Edd,C\ IV} > \lambda_{\rm Edd,Ly\alpha}$.

4.5. Composite Spectra

To further study the spectral evolution in EVQs, we construct composite spectra separately for bright and faint epochs. In this work, we use the geometric mean spectrum in order to preserve the global continuum shape, instead of the arithmetic mean spectrum, which preserves the relative fluxes of emission features. The geometric mean spectrum is generated following the procedure in Vanden Berk et al. (2001), including correcting galactic extinction, rebinning the individual spectra to the source rest frame, scaling the spectra, and finally, stacking the spectra into the composite with $\langle f_\lambda \rangle = (\prod_{i=0}^{n} f_{\lambda,i})^{1/n}$, where $f_{\lambda,i}$ is the flux of each spectrum at wavelength λ and n is the total number of spectra in spectral bins. The composite difference spectrum is also derived in a similar way. We fit composite spectra with a power law to several line-free regions between 1275 and 2400 Å (see the gray bars in Figure 8), which are the most reliable regions.

Figure 8 presents the bright, faint, and difference-composite spectra of EVQs and CLQs. The slope ($\alpha_{\rm bright} = -1.68 \pm 0.02$) of the bright EVQ composite is similar to the typical QSO spectral slope of −1.56 (Vanden Berk et al. 2001). The faint spectrum is very flat with $\alpha_{\rm faint} = -0.91 \pm 0.03$, further confirming the well-known BWB trend in quasars. Previous studies (e.g., Wilhite et al. 2005; Ruan et al. 2014; Guo & Gu 2016) have suggested that the difference spectrum slope ($\alpha_{\rm diff} = -2$) of normal QSOs is slightly shallower than the prediction of the standard disk model (e.g., $\alpha_\lambda = -2.33$, Shakura & Sunyaev 1973), likely due to the local extinction in the quasar host (Xie et al. 2016). Slopes of both difference spectra are ∼−2 in the EVQ and CLQ sample, at least indicating that the variability mechanism should be very similar among normal quasars, EVQs and CLQs.

4.6. Detection Rate

Among the total of 61,037 objects of high-redshift repeat quasars, we find 1039 objects of EVQs, uncorrected for the selection incompleteness, selection bias, and rare spurious EVQs, yielding an EVQ detection rate of ∼2%. This is broadly

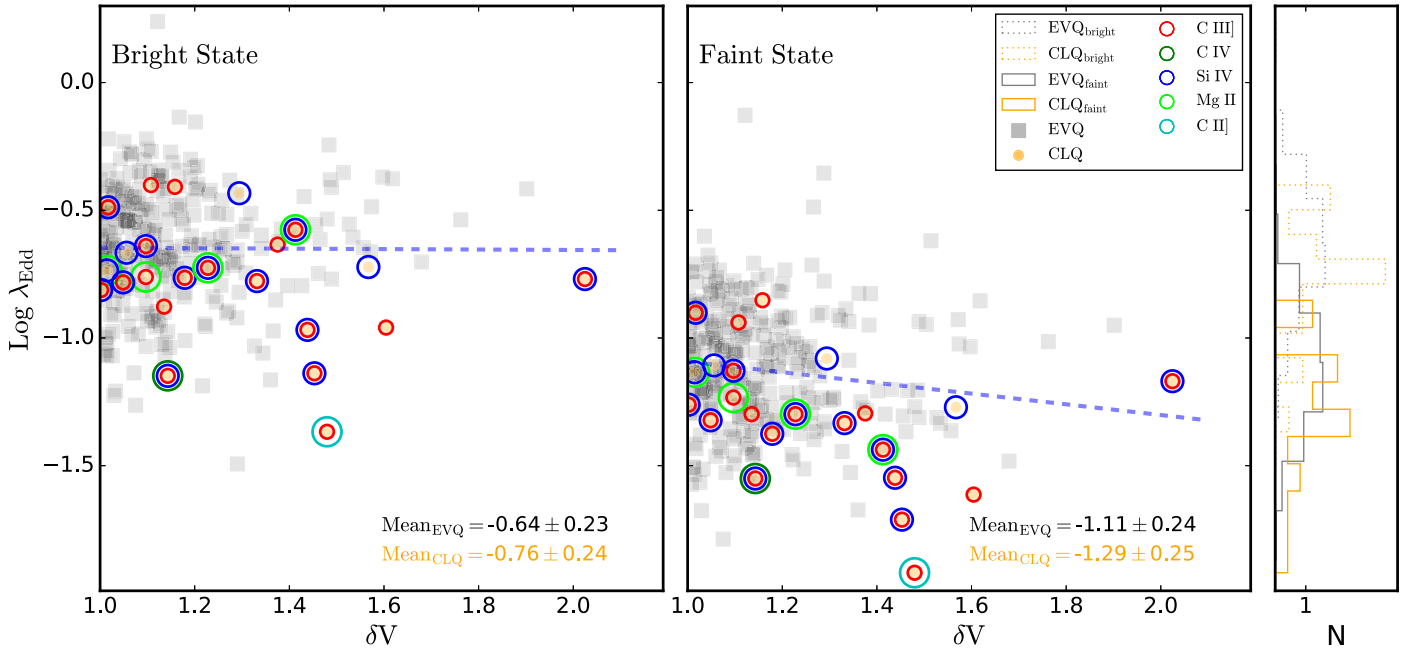

Figure 7. Eddington ratio vs. spectral variation at 1450 Å. The CLQs show a relatively lower average Eddington ratio both in bright and faint states compared to normal EVQs (also see the normalized histogram). The Eddington ratio is computed with the average BH mass of the bright/faint states, and the mean values are listed in the lower-right corner and Table 4. The whole EVQ sample shows an anticorrelation between the continuum variation and Eddington ratio with slopes of -0.01 ± 0.03 (bright) and -0.21 ± 0.05 (faint), indicated by the blue dashed lines. Different CLQs are marked with circles in different colors.

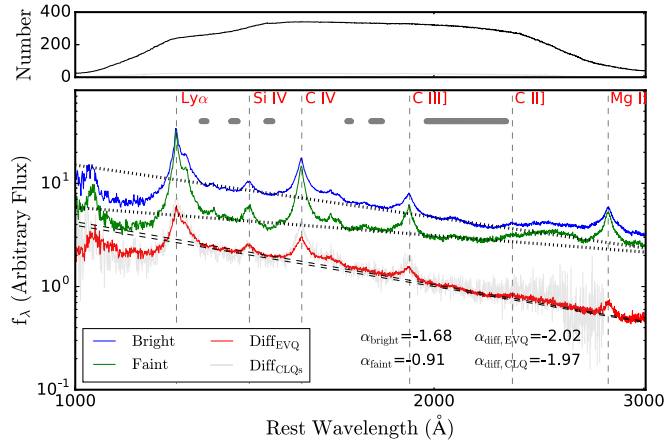

Figure 8. Geometric mean composite spectra for bright and faint states of EVQs, represented in blue and green colors in the lower panel, respectively. The red (gray) curve is the composite difference spectrum for EVQs (CLQs). All of the composite spectra are shifted for clarity. The black dashed/dotted lines are power-law fits to the line-free continuum windows (gray bars). The small upper panel shows the number of objects (black for EVQ and gray for CLQ) in each wavelength bin (1 Å) when constructing the corresponding composite spectra. Note that noisy pixels on the edges are removed during construction of the composites.

consistent with the result (∼4%, 1011 EVQs of 25,484 repeat spectra in SDSS with $|\Delta g| > 1$ mag) from MacLeod et al. (2016). However, Rumbaugh et al. (2018) reported that the EVQ fraction is about 10% with $|\Delta g| > 1$ mag based on the Stripe 82 SDSS-DES (dark energy survey; Flaugher et al. 2015) light curves. Accounting for selection effects, they further suggest an intrinsic EVQ fraction of ∼30%–50% among quasars brighter than 22 mag in the g band over a baseline of 15 yr. We suggest that the higher fraction of EVQs in the SDSS-DES search is due to the selection bias because the DES photometry is much deeper than SDSS single-epoch spectroscopic exposure.

The CLQ fraction in EVQs is about 7% (23/348), yielding a detection rate of ∼0.1% in all high-redshift repeat quasars in SDSS. This is about one order of magnitude higher than the fraction of low-redshift CLQs searched for in the same SDSS repeat spectra, e.g., ∼0.01% in Yang et al. (2018) and 0.04% in MacLeod et al. (2016). This is most likely due to the stronger variability in shorter wavelengths for high-redshift quasars.

5. Discussions

5.1. Decisive Roles for CL Behavior

Guo et al. (2020) have demonstrated that the CLQs showing the appearance/disappearance of broad emission lines with increasing/decreasing continuum is a natural phenomenon under the photoionization model. Whether the transition occurs depends primarily on several factors: (1) Eddington ratio (perhaps, although we only find a marginal clue to support it); (2) the spectral S/N of the faint state; and (3) host galaxy contamination for the low-redshift CLQs.

A quantitative photoionization calculation is shown in Figure 8 of Guo et al. (2020). While the central continuum gradually drops, the broad emission line responds to the continuum variation with a reduction of the line strength ($L_{con} \propto L_{line}$) and shrinkage of the line-emitting region, leading to a smaller emitting ring and faster rotational velocity of broad-line-emitting clouds (i.e., breathing model). When the continuum luminosity (or the Eddington ratio) is low enough assuming a constant BH mass, the broad emission line will be too weak (or too broad) to be detected, resulting in CL behavior. This simple theoretical model is in agreement with the statistical result in Figure 7, which shows that CLQ Eddington ratios are on average lower than that of normal EVQs, although the

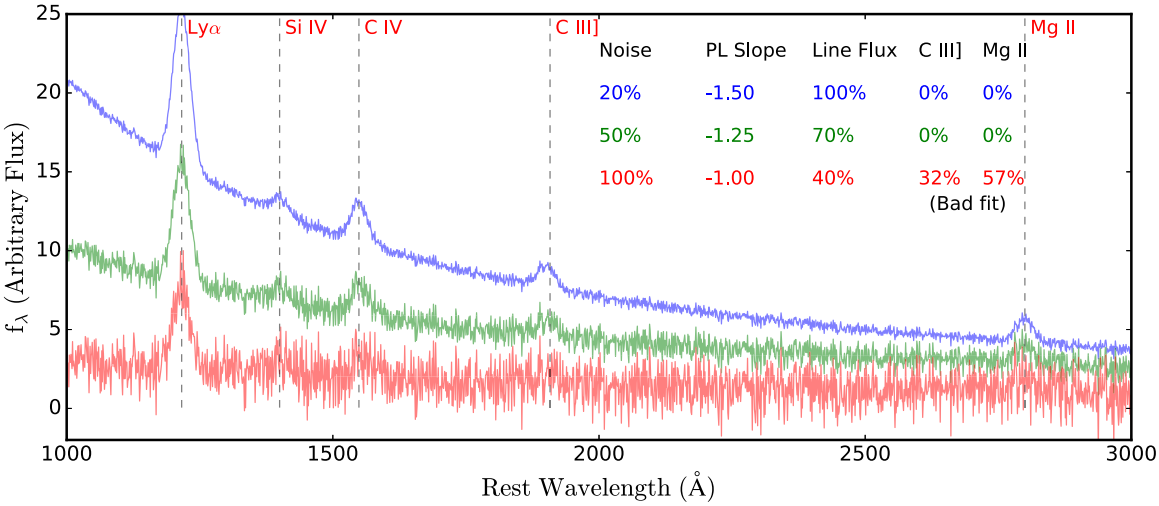

Figure 9. Simulated CLQs with increasing noise level, flattening slopes and fading line luminosities. Each spectrum consists of a continuum power law, multi-Gaussian profiles, and random Gaussian noise. With decreasing continuum emission, the broad component of each line becomes more and more illegible. The line (i.e., C III] and Mg II) fitting results for 1000 simulated spectra are listed, indicating the CL phenomenon strongly depends on the noise level with fading line flux.

significance of the difference is less than the 1σ level. In contrast, the observed C IV shows an antibreathing mode due to the nonreverberating component, we argue that the IBC may just need more time to show the breathing at further distances (Denney 2012).

Moreover, the spectral noise will dilute the weak broad component, as shown in Figure 9. We conduct a simple simulation assuming increasing Gaussian noise levels, flattening power-law slopes, and decreasing line fluxes with fading continuum at three levels. The emission lines are modeled by single-Gaussian profiles with a fixed FWHM of 5000 km s^{-1}. Each level is simulated for 1000 times with random Gaussian noise ($\mu = 0$ and σ up to 1). Then, we use `PyQSOFit` to fit each spectrum with a continuum power law and two Gaussian profiles for C III] and Mg II with a maximum line width of 10,000 km s^{-1}. In the faintest state, we find 32% and 57% of the modeled profiles hit the boundary, which means the automatic code is almost unable to correctly recognize the broad component, although the line flux is not zero. Consequently, we may classify those objects as a C III] or Mg II CLQ, whose weak broad components are actually swamped by spectral noise.

This raises an important question: what if some EVQs are classified as CLQs due to the S/N problem in our work? We stress that all previously discovered CLQs are subject to the S/N issue, and our previous analysis are based on the frame of SDSS resolution. It is possible to resolve hidden broad components with better telescopes, which is exactly the reason why we need to push to the limit to inspect the smoothed SDSS spectra for CLQ searches (e.g., in Figure 2). Because of the changeable classification of CLQs under different scenarios, we suggest that using a strict definition to differentiate CLQs and EVQs may not a good choice.

Finally, the broad emission lines (e.g., Hα and Hβ) at low redshift are more easily swamped in their bright host galaxy. However, the host contamination in our high-redshift example is negligible.

5.2. Line Transition Order in CLQs

We suggest that the intrinsic line intensity mostly determines the transition order of different lines, while the other factors (e.g., spectral S/N) are second-order effects, which may slightly exchange the order of some lines with similar intensity (e.g., C III] and Mg II; also see Table 5). In low-redshift CLQs (e.g., MacLeod et al. 2016; Yang et al. 2018), the weakest high-order broad Balmer lines (e.g., Hγ) usually disappears first, then relatively stronger Hβ, finally to the strongest Hα. In addition, the broad Mg II is usually more persistent than Hβ but seems less persistent than Hα(e.g., see the Mg II CLQ in Guo et al. 2019). In high-redshift CLQs, the UV lines (see Figures 2 and B1–B3) also basically follow this rule, e.g., C II] > Si IV and C III] and Mg II > C IV > Lyα, disappearing from first to last. Despite the line intensity of Si IV being slightly smaller than that of Mg II and C III], it does not seem to disappear significantly earlier than C III] and Mg II in most of our CLQs.

The decay rate of different lines is another factor that might have an influence on the transition order of CLQs. We mimic a quasar emission-line flux changing with its decreasing continuum within the photoionization frame following Guo et al. (2020). The basic idea is that with decreasing inputs of hydrogen-ionizing photons assuming a locally optimally emitting cloud (LOC) model (Baldwin et al. 1995), we can track the variation of the emission lines. The details of the model setup are specified in Guo et al. (2020). Figure 10 illustrates the different decay rates with a fading continuum. The gray shadow brackets the average continuum variation range in the bright and faint states of EVQs (see Figure 4).

Table 5
Line Relative Flux

Name	Vacuum λ (Å)	Rel.Flux 100× F/F(Ly α)	Sim. Flux 100× F/F(Ly α)	Decay rate (dex)
Ly α	1215.67	100	100	0.40
Si IV	1396.76	8.92	6.31	0.50
C IV	1549.06	25.29	22.38	0.45
C III]	1908.73	15.94	10.00	0.40
Mg II	2798.75	14.73	11.22	0.30

Note. The relative flux is derived from the quasar composite in Vanden Berk et al. (2001), and the simulated flux and decay rate are calculated from the photoionization model ranging from 43.8 to 43.3 erg s^{-1} following Guo et al. (2020) (also see Figure 10).

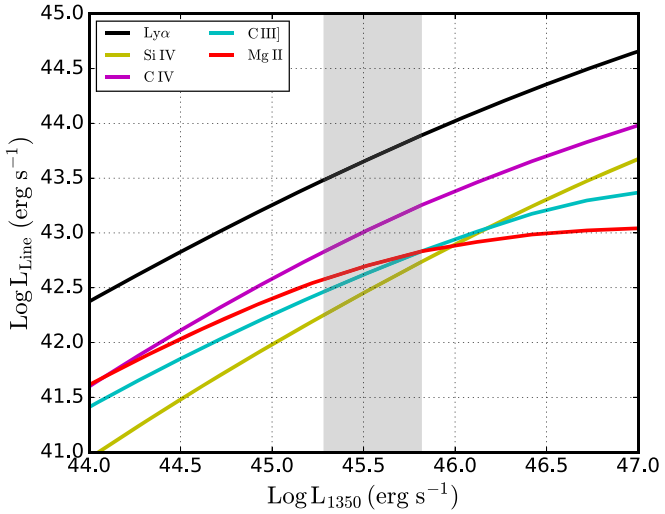

Figure 10. The simulated emission-line decay rate in the photoionization frame. The gray region of [45.3, 45.8] erg s^{-1} is our fiducial luminosity coverage according to the medians of the bright/faint continuum luminosity distribution in Figure 4. The line ratios relative to Lyα at 45.5 erg s^{-1} are listed in Table 5.

However, within the limited variability range (e.g., only 0.5 dex in the *x*-axis), the discrepancy is negligible (the quantities are listed in Table 5). Note that the less variable Mg II compared to other UV lines is also recovered (Goad et al. 1993).

5.3. Relation between EVQ and CLQ

We have demonstrated that CLQs generally have similar properties (Figures 4 and 7) compared to normal EVQs, but perhaps with slightly lower continuum luminosities and broader line widths, and hence lower Eddington ratios. Moreover, the difference-composite slopes of EVQs/CLQs in Figures 8 are both identical to those of normal quasars, indicating that they are dominated by a similar variability mechanism (also see Noda & Done 2018). The K-S test in Table 4 also suggests that EVQs and CLQs likely belong to the same population. Therefore, we conclude that CLQs and EVQs are basically the same population. Whether the broad component fully disappeared or is just too weak to be detectable also strongly depends on the spectral S/N, as shown in Figure 9. Even if the line core of a strong broad emission-line transitions into an absorption line, the broad component (line wing) may still exist (e.g., C III] in ID = 234455 in Figure B3) but is possibly too weak to be decomposed from the host component. Thus, the CLQs are just an observational class, and we recommend using EVQ instead to refer to the entire extreme variable quasar population because it is more physical.

5.4. Variability Mechanism

The AGN variability mechanism is still poorly understood. Our discovery of a bunch of high-redshift CLQs further challenges the standard disk model, which requires a variability timescale of thousands of years. It was suggested that the observed optical light curve is a mixture of various timescale variabilities that originated from the accretion disk (e.g., Cai et al. 2016; Lawrence 2018). The standard thin-disk model is expected to control the very long-term variation with a viscous timescale of 10^5 yr, while the short-term variation (days to years) is dominated by other mechanisms, e.g., the X-ray reprocessing (e.g., Krolik et al. 1991), the local temperature fluctuation in the disk (Dexter & Agol 2011; Cai et al. 2016), and corona-heated accretion disk reprocessing (Sun et al. 2020).

Through an investigation of the CLQ Mrk 1018, Noda & Done (2018) suggest that the CLQ is more likely triggered by a rapid mass accretion rate drop, accompanied by a state transition (also see Ruan et al. 2019). They point out that the sound speed could be much faster when considering a radiation-pressure-dominated disk and the magnetic pressure to help stabilize the disk (Jiang et al. 2013), which could alleviate the timescale problem. However, Lawrence (2018) indicate that the standard viscous accretion disk models are close to the edge and simply cranking up the viscosity parameter would not solve the timescale problem. The extreme reprocessing where an erratically variable central quasi-point source is entirely responsible for heating an otherwise cold and passive low-viscosity disk may be a better route forward.

5.5. C IV Line Profile

AGN broad emission lines are usually dominated by the photoionization from the accretion continuum. As mentioned, the virialized broad-line-emitting clouds will respond to the increase of the central continuum luminosity by increasing the average distance of the accompanying clouds and decreasing the average line width, known as the AGN breathing model (e.g., Guo et al. 2020). This validates some empirical single-epoch BH estimators assuming the virial motion of the clouds, in particular the Hβ for low-redshift AGNs.

C IV is the only broad emission line widely used to estimate the BH mass at high redshift (i.e., $z > 2.3$). However, the antibreathing of C IV results in a luminosity-independent BH mass with a discrepancy of 0.3 dex in bright and faint states as shown in Section 4.3, challenging the widely used empirical mass estimator (Vestergaard & Peterson 2006). The antibreathing of C IV is usually explained by the presence of a nonvarying core component in addition to a reverberating broad-base component (Denney 2012), consistent with the behavior in Figure 5. Previous studies speculate that the nonreverberating core component is more likely associated with a disk wind (e.g., Proga et al. 2000) or originates from an intermediate-line region (e.g., Wills et al. 1993), commonly accompanied by a blueshift relative to the systemic velocity of the quasar (Richards et al. 2002; Sun et al. 2018).

Among our 348 objects, 244 show the antibreathing behavior, and 104 present the expected breathing mode, indicating that antibreathing dominates the C IV variability, but normal-breathing C IV still exists. To date, there is still no ideal solution to fix the BH mass discrepancy in bright and faint states, although previous work tried to recalibrate the C IV-based BH mass to that from Hβ, e.g., using an ultraviolet (or Eigenvector 1) indicator: the line peak flux ratio of Si IV and C IV (Runnoe et al. 2013). Therefore, we use the mean value as our fiducial BH mass from C IV. Note that the variability introduces the extra scatter of 0.3 dex for C IV-based BH mass, which is already nonnegligible compared with the systematic scatter of ~0.4 dex uncertainty in single-epoch mass estimates (Shen 2013).

Wang et al. (2020) have suggested that Hβ (and to a lesser extent, Hα) displays the most consistent normal breathing

expected from the virial relation, Mg II mostly shows no breathing (also see Shen 2013; Yang et al. 2020), and C IV (and similarly C III]) mostly shows antibreathing (Wills et al. 1993; Denney 2012). The BH mass based on Mg II should be more precise than the C IV BH mass (Shen et al. 2008; Shen & Liu 2012). However, the Mg II lines in most EVQs are too noisy due to the faintness of our sample and approaching/exceeding the edge of wavelength coverage of the SDSS spectra.

6. Conclusions

We have compiled a sample of 348 spectroscopically selected EVQs at redshift >1.5 with repeat observations (Nepoch $\geqslant 2$) from SDSS DR16. The continuum variability at 1450 Å between the brightest and faintest epochs in each object is larger than 100%, i.e., $\delta V \equiv (\mathrm{Max}-\mathrm{Min})/\mathrm{Mean} > 1$. Among those 348 EVQ objects, we have discovered 23 high-redshift CLQs (Figure 2 and B1–B3) with transitions in distinctive broad emission lines (e.g., C III], Mg II), yielding a detection rate of ~7% in EVQs. We caution that the problematic spectral flux calibration of SDSS spectrum (i.e., fiber-drop epoch) may mimic the faint state of a CLQ (Figure A2). We explore the properties of EVQs and CLQs; the main findings are as follows:

1. Through the comparison of various properties, i.e., continuum/line properties (Figure 4), composites (Figure 8), and Eddington ratio (Figure 7), we conclude that EVQs and CLQs are basically the same population, as a tail of a continuous distribution of normal quasar properties (Rumbaugh et al. 2018). Further dividing the observed CLQs and EVQs with a strict and clean definition is not easy due to spectral noise (Figure 9).
2. We originally expect that the CLQs are a subset of EVQs with less efficient accretion. However, our Eddington ratio distributions (Figure 7) show no reliable evidence to support that, with a confidence level of $\lesssim 1\sigma$, regardless of other potential biases.
3. The disappearance order of different UV emission lines in high-redshift CLQs generally dominated by line intensity (Table 5) basically follows C II] > Si IV and C III] and Mg II > C IV > Lyα (disappearing from first to last). The line decay rate (Figure 10) and host contamination have little influence on the transition order.
4. The antibreathing behavior (i.e., $L_{\mathrm{con}} \propto \mathrm{FWHM}$) of C IV is confirmed in our EVQ sample, which is caused by a relatively narrow nonreverberating component probably originating from a disk wind (Proga et al. 2000) or an intermediate-line region (Wills et al. 1993). We caution that due to the antibreathing of C IV, extreme AGN variability will introduce an extra BH mass scatter of ~0.3 dex at $L_{1350} \sim 45.5$ erg s^{-1}, which is comparable to the systematic scatter of ~0.4 dex with the empirical single-epoch estimator.

The variability mechanism of CLQs/EVQs will continue to be a primary issue in the near future. Multiwavelength data (e.g., UV/optical and X-ray) and a large sample of CLQs (e.g., even faint CLQs of C IV and Ly α) will be helpful to understand quasar variability more generally. In addition, theoretical calculations based on the LOC model by connecting concurrent X-ray and UV/optical data may further unveil the mystery of quasar variability.

We thank the referee, Yue Shen and Zhenyi Cai, for constructive comments that improved the paper. H.X.G. is supported by NSF grant AST-1907290. C.J.B. acknowledges support from the Illinois graduate survey science fellowship. M.Y.S. acknowledges support from the National Natural Science Foundation of China (NSFC-11973002). Z.C.H. is supported by NSFC-11903031 and USTC Research Funds of the Double First-Class Initiative. T.G.W. is supported by NSFC-11833007. M.F.G. is supported by NSFC-11873073. M. Z.K. is supported by the Joint Research Fund in Astronomy (No. U1831126) under cooperative agreement between the NSFC and CAS and Natural Science Foundation of Hebei Province No. A2019205100.

SDSS-IV is managed by the Astrophysical Research Consortium for the Participating Institutions of the SDSS Collaboration including the Brazilian Participation Group, the Carnegie Institution for Science, Carnegie Mellon University, the Chilean Participation Group, the French Participation Group, Harvard-Smithsonian Center for Astrophysics, Instituto de Astrofísica de Canarias, The Johns Hopkins University, Kavli Institute for the Physics and Mathematics of the Universe (IPMU)/University of Tokyo, Lawrence Berkeley National Laboratory, Leibniz Institut für Astrophysik Potsdam (AIP), Max-Planck-Institut für Astronomie (MPIA Heidelberg), Max-Planck-Institut für Astrophysik (MPA Garching), Max-Planck-Institut für Extraterrestrische Physik (MPE), National Astronomical Observatories of China, New Mexico State University, New York University, University of Notre Dame, Observatário Nacional/MCTI, The Ohio State University, Pennsylvania State University, Shanghai Astronomical Observatory, United Kingdom Participation Group,Universidad Nacional Autónoma de México, University of Arizona, University of Colorado Boulder, University of Oxford, University of Portsmouth, University of Utah, University of Virginia, University of Washington, University of Wisconsin, Vanderbilt University, and Yale University.

Software: Astropy (Astropy Collaboration et al. 2013), Matplotlib (Hunter 2007), Numpy and Scipy (van der Walt et al. 2011), Pysynphot (STScI Development Team 2013), PyQSOFit (Guo et al. 2018).

Appendix A
Spectral Flux-calibration Problem

Each SDSS spectrum is flux-calibrated by matching the counts in the mean of the high-S/N spectra of the spectrophotometric and reddening standards on the plate and equating this to the synthetic composite F8 subdwarf spectrum. This is placed on an absolute scale by matching the synthesized magnitudes of these stars to the SDSS photometry. Based on previous studies, two important aspects should be considered regarding the SDSS spectral variability: (1) the original uncertainties of the SDSS spectral flux calibration (Figure A1) and (2) the fiber-drop issue (i.e., the fiber is partially dropped from a plate, resulting in a significant drop in spectral flux; see Figure A2).

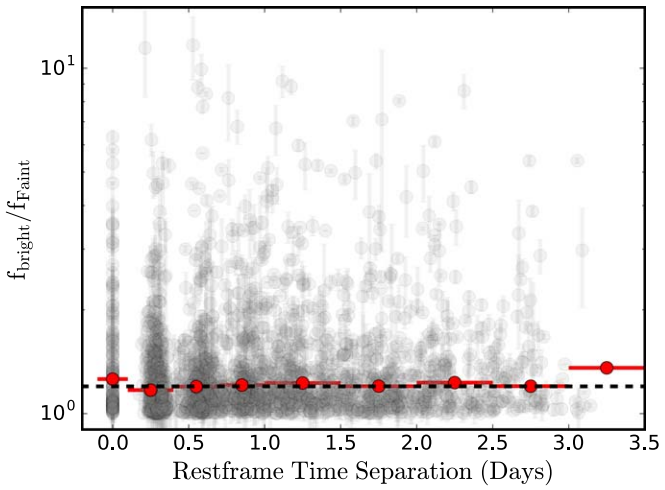

Figure A1. Rest-frame time separation vs. continuum flux ratio at 1450 Å. The gray dots are 2400 high-redshift ($z > 1.5$), two-epoch radio-quiet quasars with observed time separation less than 10 days. The red dots are the median values in different bins (horizontal error bars), and the black dashed line is the uncertainty level of 20%.

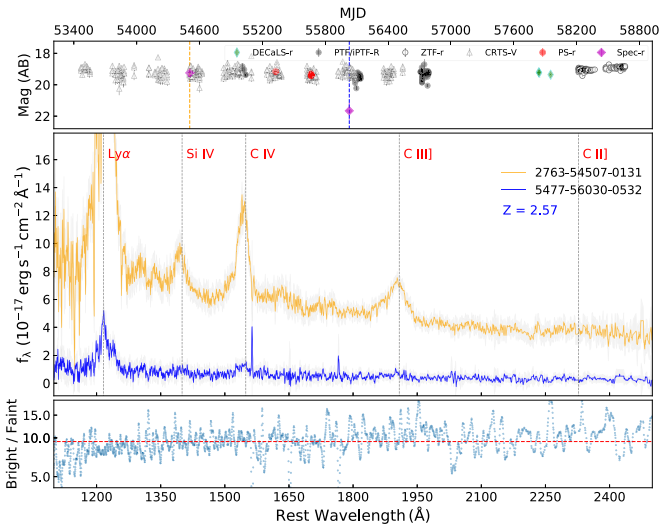

Figure A2. Example of a fiber-drop quasar which mimics a C III] and/or C IV CLQ. The synthetic magnitude from the blue spectrum (MJD = 56030) is >2 mag fainter than concurrent multisurvey photometries, indicating a problematic epoch with a dropped fiber rather than a true variability within such a short timescale. The spectral ratio of the bright and faint states is also shown in the bottom panel.

A.1. Intrinsic Scatter

The asserted accuracy of the spectrophotometric calibration of stars is about 6% in SDSS. However, we find that the accuracy of the spectrophotometry for high-redshift quasars (point source) based on repeat spectra is around 20% in Figure A1, consistent with Stoughton et al. (2002). To evaluate the flux-calibration accuracy of SDSS spectra at high redshift, we compile a sample of 2400 two-epoch radio-quiet normal quasars ($z > 1.5$) with time separation $\Delta T < 10$ days in the observed frame and presents the time separation between the bright and faint epochs in rest-frame versus continuum flux ratio at 1450 Å in Figure A1. The normal quasar variability on a timescale of 10 days is around 0.02 mag (5% in flux) according to the structure function of Stripe 82 quasars (MacLeod et al. 2010). However, we surprisingly find that about 1% of objects show a continuum variation ($f_{\rm bright}/f_{\rm faint}$) larger than 500%, even for the same-night observations. The median flux ratios in different bins are about 20%, consistent with the believed accuracy in Stoughton et al. (2002). In addition, we speculate that objects with very large flux ratios (e.g., >500%) are subject to the fiber-drop issue (see Section A.2) to different degrees. The apparent anticorrelation between the flux ratio and time separation is not real because fewer objects are distributed around 3 days.

A.2. Fiber-drop Epochs

The scenario becomes even worse when a fiber is inadvertently loose or partially dropped for high-redshift objects without any caution or flag from the SDSS pipeline. This very rare phenomenon was also confirmed in repeatedly monitored TDSS and SDSS-RM programs (Shen et al. 2015; Sun et al. 2015). As shown in Figure A2, a partially fiber-dropped epoch (faint blue epoch, middle panel) mimics a C III] and/or C IV CLQ with a significant drop of continuum flux. The synthetic magnitude for the faint spectrum totally disobeys the concurrent photometries and typical short-term variability magnitude. In addition to simultaneous photometries, a fiber-drop spectrum usually has an identical shape (i.e., continuum slope and line profile) to the bright state, rather than showing a BWB trend as a typical quasar, which is further demonstrated by the flat spectral ratio of bright and faint states (bottom panel). Moreover, with a typical exposure time (45 minutes) for SDSS objects, the S/N for the faint state is usually much lower than that of the bright state with such a huge variation, rather than similar S/Ns in both states.

Appendix B
The Rest of the CLQs

The rest of the CLQs of Figure 2 are shown in Figures B1–B3.

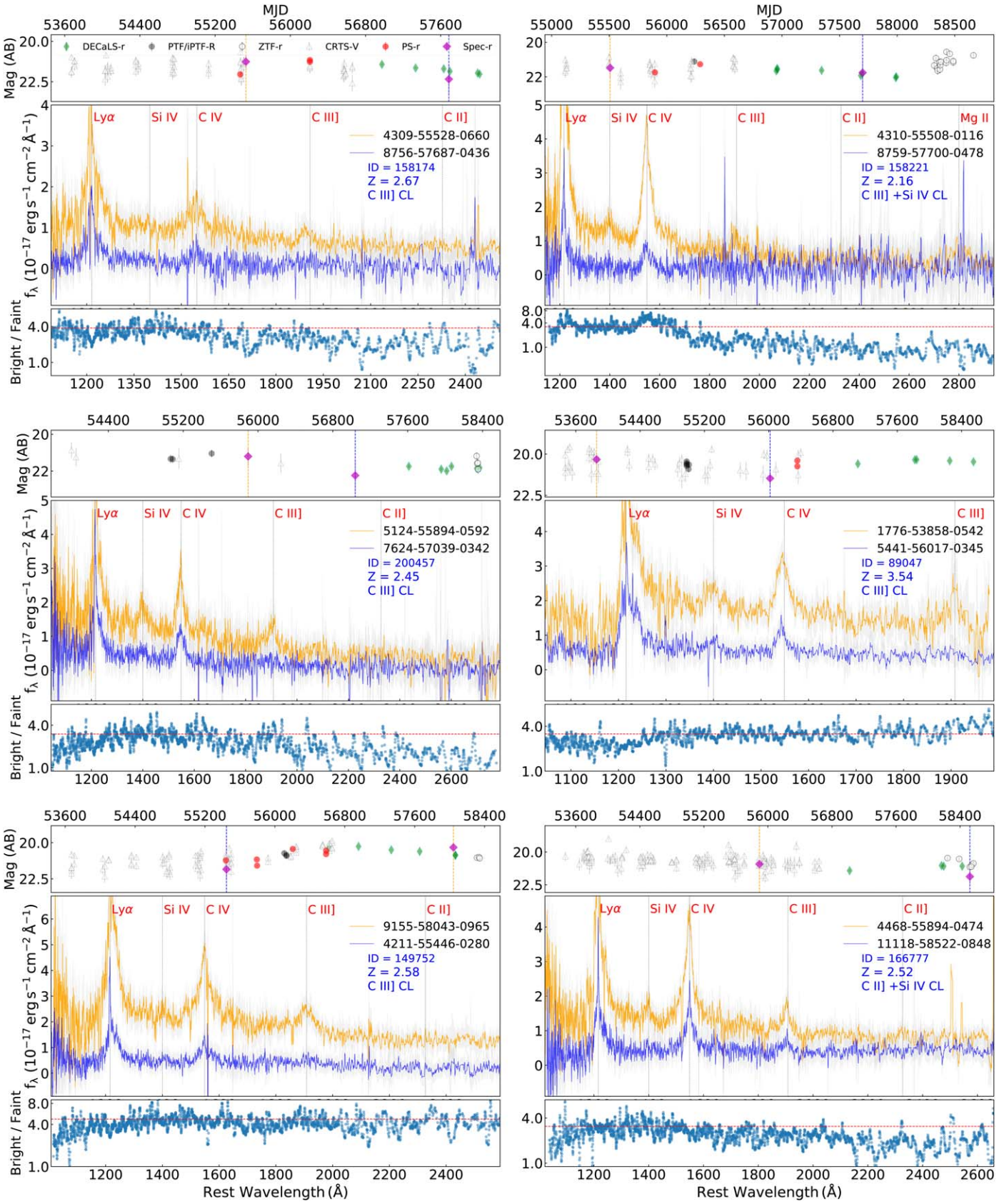

Figure B1. See Figure 2.

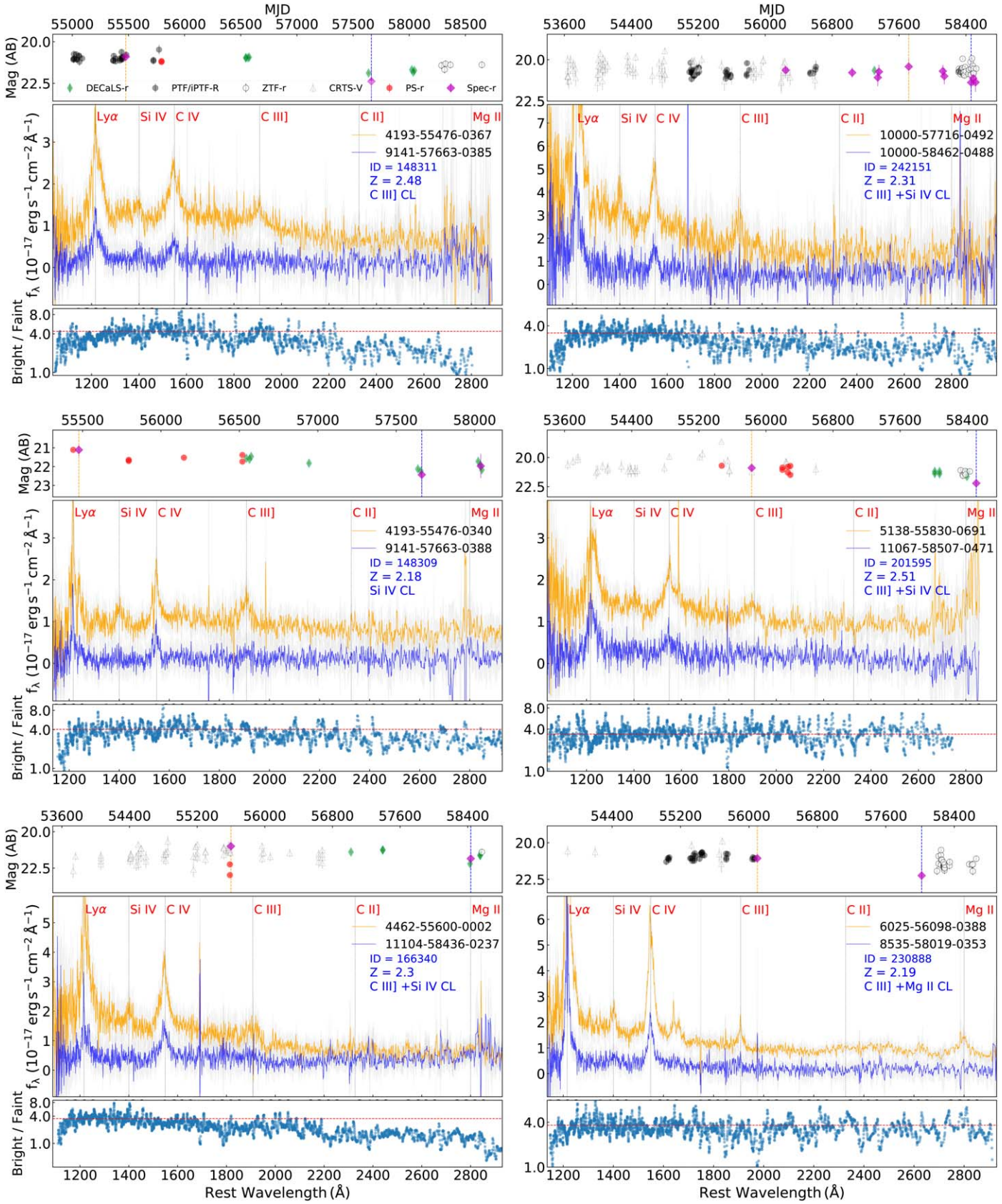

Figure B2. See Figure 2.

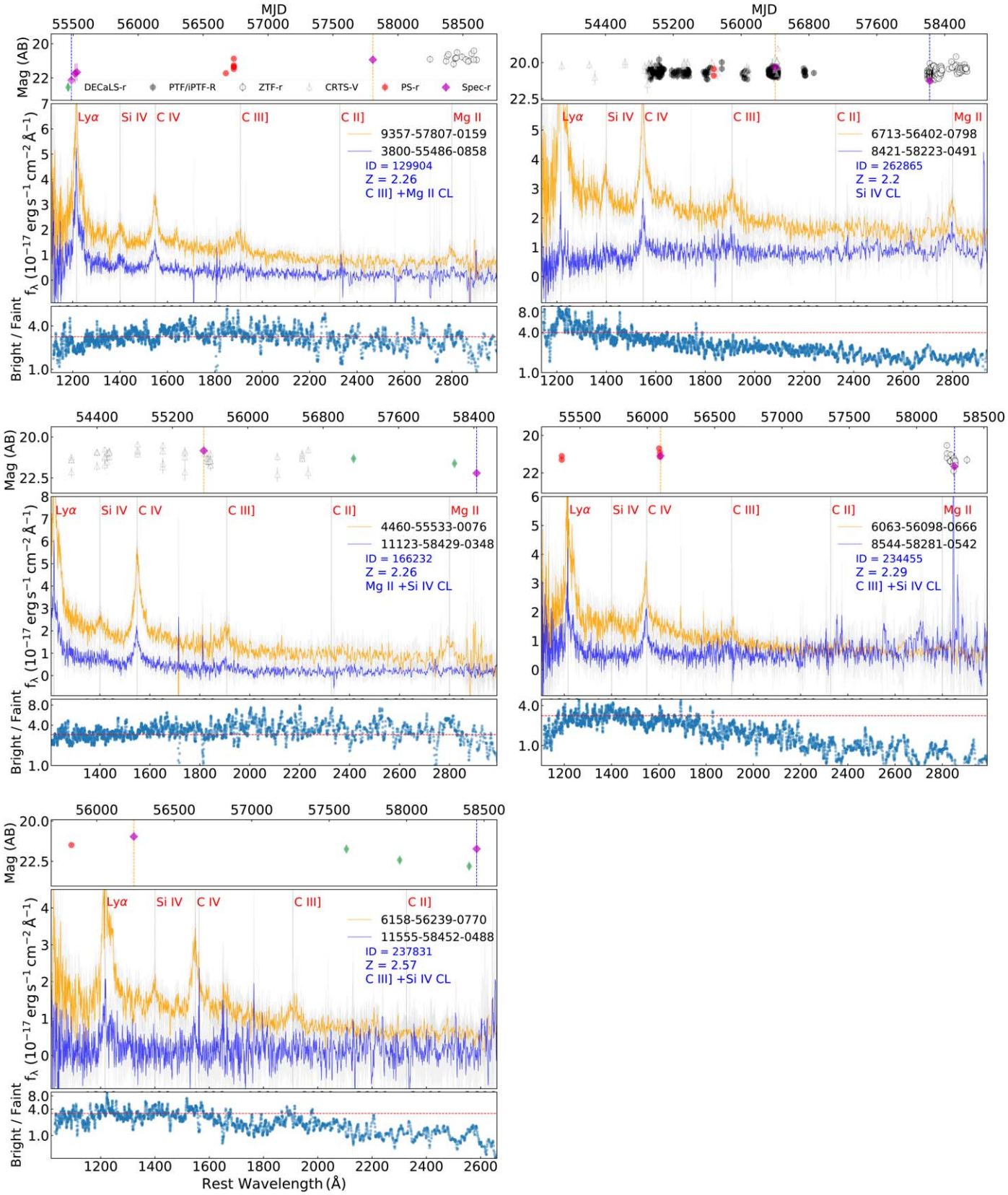

Figure B3. See Figure 2.

ORCID iDs

Hengxiao Guo (郭恒潇) https://orcid.org/0000-0001-8416-7059
Colin J. Burke https://orcid.org/0000-0001-9947-6911
Mouyuan Sun https://orcid.org/0000-0002-0771-2153
Zhenfeng Sheng https://orcid.org/0000-0001-6938-8670
Tinggui Wang https://orcid.org/0000-0002-1517-6792
Zhicheng He https://orcid.org/0000-0003-3667-1060
Minfeng Gu https://orcid.org/0000-0002-4455-6946

References

Ahumada, R., Allende Prieto, C., Almeida, A., et al. 2020, ApJS, 249, 3
Ai, Y., Dou, L., Yang, C., et al. 2020, ApJL, 890, L29
Ai, Y. L., Yuan, W., Zhou, H. Y., et al. 2010, ApJL, 716, L31
Antonucci, R. 1993, ARA&A, 31, 473
Aretxaga, I., Joguet, B., Kunth, D., Melnick, J., & Terlevich, R. J. 1999, ApJL, 519, L123
Astropy Collaboration, Robitaille, T. P., Tollerud, E. J., et al. 2013, A&A, 558, A33
Baldwin, J., Ferland, G., Korista, K., & Verner, D. 1995, ApJL, 455, L119
Baldwin, J. A. 1977, ApJ, 214, 679
Barth, A. J., Bennert, V. N., Canalizo, G., et al. 2015, ApJS, 217, 26
Bellm, E. C., Kulkarni, S. R., Graham, M. J., et al. 2019, PASP, 131, 018002
Bolton, A. S., Schlegel, D. J., Aubourg, É., et al. 2012, AJ, 144, 144
Cackett, E. M., & Horne, K. 2006, MNRAS, 365, 1180
Cai, Z., Sun, Y., Wang, J., et al. 2019, SCPMA, 62, 69511
Cai, Z.-Y., Wang, J.-X., Gu, W.-M., et al. 2016, ApJ, 826, 7
Chambers, K. C., Magnier, E. A., Metcalfe, N., et al. 2016, arXiv:1612.05560
Cohen, R. D., Rudy, R. J., Puetter, R. C., Ake, T. B., & Foltz, C. B. 1986, ApJ, 311, 135
Cui, X.-Q., Zhao, Y.-H., Chu, Y.-Q., et al. 2012, RAA, 12, 1197
Dawson, K. S., Kneib, J.-P., Percival, W. J., et al. 2016, AJ, 151, 44
Denney, K. D. 2012, ApJ, 759, 44
Denney, K. D., De Rosa, G., Croxall, K., et al. 2014, ApJ, 796, 134
Denney, K. D., Peterson, B. M., Dietrich, M., Vestergaard, M., & Bentz, M. C. 2009, ApJ, 692, 246
DESI Collaboration, Aghamousa, A., Aguilar, J., et al. 2016, arXiv:1611.00036
Dexter, J., & Agol, E. 2011, ApJL, 727, L24
Dexter, J., & Begelman, M. C. 2019, MNRAS, 483, L17
Dey, A., Schlegel, D. J., Lang, D., et al. 2019, AJ, 157, 168
Drake, A. J., Catelan, M., Djorgovski, S. G., et al. 2013, ApJ, 763, 32
Drake, A. J., Djorgovski, S. G., Mahabal, A., et al. 2009, ApJ, 696, 870
Eracleous, M., Boroson, T. A., Halpern, J. P., & Liu, J. 2012, ApJS, 201, 23
Flaugher, B., Diehl, H. T., Honscheid, K., et al. 2015, AJ, 150, 150
Goad, M. R., O'Brien, P. T., & Gondhalekar, P. M. 1993, MNRAS, 263, 149
Goodrich, R. W. 1989, ApJ, 340, 190
Graham, M. J., Ross, N. P., Stern, D., et al. 2020, MNRAS, 491, 4925
Gravity Collaboration, Sturm, E., Dexter, J., et al. 2018, Natur, 563, 657
Guo, H., & Gu, M. 2014, JApA, 35, 477
Guo, H., & Gu, M. 2016, ApJ, 822, 26
Guo, H., Shen, Y., He, Z., et al. 2020, ApJ, 888, 58
Guo, H., Shen, Y., & Wang, S. 2018, PyQSOFit: Python code to fit the spectrum of quasars, Astrophysics Source Code Library, ascl:1809.008
Guo, H., Sun, M., Liu, X., et al. 2019, ApJL, 883, L44
Homan, D., MacLeod, C. L., Lawrence, A., Ross, N. P., & Bruce, A. 2020, MNRAS, 496, 309
Hunter, J. D. 2007, CSE, 9, 90
Hutchinson, T. A., Bolton, A. S., Dawson, K. S., et al. 2016, AJ, 152, 205
Hutsemékers, D., Agís González, B., Marin, F., et al. 2019, A&A, 625, A54
Hutsemékers, D., Agís González, B., Sluse, D., Ramos Almeida, C., & Acosta Pulido, J. A. 2017, A&A, 604, L3
Jiang, L., Fan, X., Ivezić, Ž, et al. 2007, ApJ, 656, 680
Jiang, L., Fan, X., & Vestergaard, M. 2008, ApJ, 679, 962
Jiang, Y.-F., Stone, J. M., & Davis, S. W. 2013, ApJ, 778, 65
Kollmeier, J. A., Zasowski, G., Rix, H.-W., et al. 2017, arXiv:1711.03234
Korista, K. T., & Goad, M. R. 2000, ApJ, 536, 284
Krolik, J. H., Horne, K., Kallman, T. R., et al. 1991, ApJ, 371, 541
LaMassa, S. M., Cales, S., Moran, E. C., et al. 2015, ApJ, 800, 144
Law, N. M., Kulkarni, S. R., Dekany, R. G., et al. 2009, PASP, 121, 1395
Lawrence, A. 2018, NatAs, 2, 102
Liu, X., Dittmann, A., Shen, Y., & Jiang, L. 2018, ApJ, 859, 8
Liu, X., Shen, Y., Bian, F., Loeb, A., & Tremaine, S. 2014, ApJ, 789, 140
Luo, Y., Shen, Y., & Yang, Q. 2020, MNRAS, 494, 3686
MacLeod, C. L., Green, P. J., Anderson, S. F., et al. 2019, ApJ, 874, 8
MacLeod, C. L., Ivezić, Ž, Kochanek, C. S., et al. 2010, ApJ, 721, 1014
MacLeod, C. L., Ross, N. P., Lawrence, A., et al. 2016, MNRAS, 457, 389
Masci, F. J., Laher, R. R., Rusholme, B., et al. 2019, PASP, 131, 018003
Noda, H., & Done, C. 2018, MNRAS, 480, 3898
Proga, D., Stone, J. M., & Kallman, T. R. 2000, ApJ, 543, 686
Rau, A., Kulkarni, S. R., Law, N. M., et al. 2009, PASP, 121, 1334
Richards, G. T., Fan, X., Newberg, H. J., et al. 2002, AJ, 123, 2945
Richards, G. T., Lacy, M., Storrie-Lombardi, L. J., et al. 2006, ApJS, 166, 470
Roig, B., Blanton, M. R., & Ross, N. P. 2014, ApJ, 781, 72
Ross, N. P., Graham, M. J., Calderone, G., et al. 2020, MNRAS, 498, 2339
Ruan, J. J., Anderson, S. F., Cales, S. L., et al. 2016b, ApJ, 826, 188
Ruan, J. J., Anderson, S. F., Dexter, J., & Agol, E. 2014, ApJ, 783, 105
Ruan, J. J., Anderson, S. F., Eracleous, M., et al. 2019, ApJ, 883, 76
Ruan, J. J., Anderson, S. F., Green, P. J., et al. 2016a, ApJ, 825, 137
Rumbaugh, N., Shen, Y., Morganson, E., et al. 2018, ApJ, 854, 160
Runco, J. N., Cosens, M., Bennert, V. N., et al. 2016, ApJ, 821, 33
Runnoe, J. C., Brotherton, M. S., Shang, Z., & DiPompeo, M. A. 2013, MNRAS, 434, 848
Runnoe, J. C., Cales, S., Ruan, J. J., et al. 2016, MNRAS, 455, 1691
Runnoe, J. C., Eracleous, M., Pennell, A., et al. 2017, MNRAS, 468, 1683
Shakura, N. I., & Sunyaev, R. A. 1973, A&A, 500, 33
Shappee, B. J., Prieto, J. L., Grupe, D., et al. 2014, ApJ, 788, 48
Shen, Y. 2013, BASI, 41, 61
Shen, Y., Brandt, W. N., Dawson, K. S., et al. 2015, ApJS, 216, 4
Shen, Y., Greene, J. E., Strauss, M. A., Richards, G. T., & Schneider, D. P. 2008, ApJ, 680, 169
Shen, Y., Hall, P. B., Horne, K., et al. 2019, ApJS, 241, 34
Shen, Y., & Liu, X. 2012, ApJ, 753, 125
Shen, Y., Richards, G. T., Strauss, M. A., et al. 2011, ApJS, 194, 45
Sheng, Z., Wang, T., Jiang, N., et al. 2017, ApJL, 846, L7
Sheng, Z., Wang, T., Jiang, N., et al. 2020, ApJ, 889, 46
Stoughton, C., Lupton, R. H., Bernardi, M., et al. 2002, AJ, 123, 485
STScI Development Team 2013, pysynphot: Synthetic photometry software package, Astrophysics Source Code Library, ascl:1303.023
Sun, M., Trump, J. R., Shen, Y., et al. 2015, ApJ, 811, 42
Sun, M., Xue, Y., Brandt, W. N., et al. 2020, ApJ, 891, 178
Sun, M., Xue, Y., Cai, Z., & Guo, H. 2018, ApJ, 857, 86
Sun, Y.-H., Wang, J.-X., Chen, X.-Y., & Zheng, Z.-Y. 2014, ApJ, 792, 54
Tohline, J. E., & Osterbrock, D. E. 1976, ApJL, 210, L117
Trakhtenbrot, B., Arcavi, I., MacLeod, C. L., et al. 2019, ApJ, 883, 94
Tran, H. D., Osterbrock, D. E., & Martel, A. 1992, AJ, 104, 2072
Urry, C. M., & Padovani, P. 1995, PASP, 107, 803
van der Walt, S., Colbert, S. C., & Varoquaux, G. 2011, CSE, 13, 22
Vanden Berk, D. E., Richards, G. T., Bauer, A., et al. 2001, AJ, 122, 549
Vestergaard, M., & Peterson, B. M. 2006, ApJ, 641, 689
Wang, J., Xu, D. W., & Wei, J. Y. 2018, ApJ, 858, 49
Wang, S., Shen, Y., Jiang, L., et al. 2020, ApJ, 903, 51
Wilhite, B. C., Brunner, R. J., Grier, C. J., Schneider, D. P., & vanden Berk, D. E. 2008, MNRAS, 383, 1232
Wilhite, B. C., Vanden Berk, D. E., Brunner, R. J., & Brinkmann, J. V. 2006, ApJ, 641, 78
Wilhite, B. C., Vanden Berk, D. E., Kron, R. G., et al. 2005, ApJ, 633, 638
Wills, B. J., Brotherton, M. S., Fang, D., Steidel, C. C., & Sargent, W. L. W. 1993, ApJ, 415, 563
Xie, X., Shao, Z., Shen, S., Liu, H., & Li, L. 2016, ApJ, 824, 38
Yang, Q., Shen, Y., Chen, Y.-C., et al. 2020, MNRAS, 493, 5773
Yang, Q., Wu, X.-B., Fan, X., et al. 2018, ApJ, 862, 109